THESIS FOR THE DEGREE OF DOCTOR OF PHILOSOPHY

On the defective origin of conductive and structural properties of oxides: insights from first principles

ANDERS LINDMAN

Department of Physics
CHALMERS UNIVERSITY OF TECHNOLOGY
Göteborg, Sweden 2017

On the defective origin of conductive and structural properties of oxides: insights from first principles
ANDERS LINDMAN

ISBN 978-91-7597-587-0

Doktorsavhandlingar vid Chalmers Tekniska Högskola
Ny serie nr 4268
ISSN 0346-718X

Department of Physics
Chalmers University of Technology
SE-412 96 Göteborg, Sweden
Telephone +46 31 772 10 00

Cover: A selection of point defects at a symmetric $(111)[\bar{1}10]$ tilt grain boundary in $BaZrO_3$. From left to right: oxygen vacancy (cyan), proton (white), *B*-site acceptor dopant (yellow), and hole polaron (cyan). Green, blue and red atoms represent barium, zirconium and oxygen, respectively.

Typeset in XeLaTeX with Times Ten and Akzidenz-Grotesk. Figures have been created using matplotlib [1], OVITO [2], and Inkscape [3].

Chalmers reproservice
Göteborg, Sweden 2017

On the defective origin of conductive and structural properties of oxides: insights from first principles

ANDERS LINDMAN
Department of Physics
Chalmers University of Technology

Abstract

Oxides are versatile materials with applications in many different research fields; especially those related to clean energy technologies, such as fuel cells, batteries and solar panels. Many functional properties of these materials derive from lattice imperfections, or *defects*, and a lot of effort has been put into fine tuning these materials by modifying their structure on the atomic scale. This lays the foundation for this thesis, where the aim has been to explain the underlying mechanisms of properties in a selection of oxides, mainly those with the perovskite structure (ABO_3), by studying a variety of different defect species: *oxygen vacancies*, *protons* and *hydride ions*, *acceptor dopants*, *electron* and *hole polarons*, and *grain boundaries* (GBs). The methodology employed here constitutes a set of first-principles methods, mainly different flavors of density-functional theory (DFT) but also perturbation theory within the G_0W_0 approximation, assisted by thermodynamic modeling.

The major part of the thesis is focused on defects in $BaZrO_3$, an oxide that when acceptor-doped and exposed to water acts as one of the most promising ceramic proton conductors by combining high bulk conductivity with high thermodynamic stability. The total proton conductivity in this material is, however, limited by high impedance at GBs due to the formation of space charges at these interfaces. This issue is addressed in four of the appended papers, which include studies on several different GBs as well as a comparison with GBs in the similar perovskite $BaCeO_3$. Acceptor-doped $BaZrO_3$ is also a p-type conductor under oxidizing conditions and this serves as the motivation for two papers, which address the description of holes in these materials. The final paper on $BaZrO_3$ sets out to describe the chemical expansion the material exhibits upon hydration.

The work extends beyond conventional ceramic proton conductors with a study on the novel oxyhydride material $BaTiO_{3-x}H_x$, where the electronic and vibrational properties of hydride ions are investigated. Finally, the thesis is concluded with a study of the oxygen vacancy in a set of binary and ternary oxides, where the aim is to show the general behavior this defect displays in these materials despite the fact that both the electronic and ionic structure vary significantly between the different compounds.

Keywords: point defects, grain boundaries, space charges, polarons, oxides, proton conductors, $BaZrO_3$, oxyhydrides. density-functional theory, thermodynamic modeling.

LIST OF PUBLICATIONS

This thesis consists of an introductory text and the following papers:

- I **Origin of space charge in grain boundaries of proton-conducting $BaZrO_3$**
  Edit E. Helgee, Anders Lindman and Göran Wahnström
  Fuel Cells **13**, 19-28 (2013)
- II **Theoretical modeling of defect segregation and space-charge formation in the $BaZrO_3$ (210)[001] tilt grain boundary**
  Anders Lindman, Edit E. Helgee and Göran Wahnström
  Solid State Ionics **252**, 121-125 (2013)
- III **Defect segregation to grain boundaries in $BaZrO_3$ from first-principles free energy calculations**
  Anders Lindman, Tor S. Bjørheim and Göran Wahnström
  Journal of Materials Chemistry A, Accepted (2017)
- IV **Differences in space-charge formation at grain boundaries in $BaZrO_3$ and $BaCeO_3$**
  Edit E. Helgee, Anders Lindman and Göran Wahnström
  (In manuscript)
- V **Size and shape of oxygen vacancies and protons in acceptor-doped barium zirconate**
  Erik Jedvik, Anders Lindman, Magnús Þ. Benediktsson and Göran Wahnström
  Solid State Ionics **275**, 2-8 (2015)
- VI **Implications of the band gap problem on oxidation and hydration in acceptor-doped barium zirconate**
  Anders Lindman, Paul Erhart and Göran Wahnström
  Physical Review B **91**, 245114 (2015)
- VII **Polaronic contributions to oxidation and hole conductivity in acceptor-doped $BaZrO_3$**
  Anders Lindman, Paul Erhart and Göran Wahnström
  Physical Review B **94**, 075204 (2016)

VIII **Vibrational characterization of electronic defects in oxyhydride barium titanate**
Erik Jedvik Granhed, Anders Lindman, Carin Österberg, Maths Karlsson and Göran Wahnström
(In manuscript)

IX **A unifying perspective on oxygen vacancies in wide band gap oxides**
Christopher Linderälv, Anders Lindman, and Paul Erhart
(In manuscript)

The author's contributions to the papers:

I The author did part of the calculations and the space-charge modeling, and assisted in writing the paper.

II The author performed the calculations and space-charge modeling, and wrote the paper.

III The author did the DFT and phonon calculations. The paper was written jointly.

IV The author and Edit E. Helgee performed in equal parts the calculations and the space-charge modeling. The analysis and the writing of the paper were done jointly.

V The author assisted with the calculations and with the analysis. The paper was written jointly.

VI The author did the DFT calculations and the thermodynamic modeling, and wrote the paper.

VII The author did the calculations and wrote the paper.

VIII The author provided help with the choice of approach and method, and assisted in writing the paper.

IX The author did part of the calculations and assisted with the analysis and in writing the paper.

Publications not included in the thesis:

Oxygen vacancy segregation in grain boundaries of $BaZrO_3$ using interatomic potentials
Anders Lindman, Edit E. Helgee, B. Joakim Nyman and Göran Wahnström
Solid State Ionics **230**, 27-31 (2013)

Contents

1

Introduction and motivation

Today, the global society relies on the use and production of fossil fuels. This has a negative impact on the environment in terms of pollution as well as global warming due to emission of greenhouse gases. There are also economic and political aspects of concern here as most of the world's oil deposits are limited to relatively few geographical areas, many which lie in unstable regions. In addition, a significant amount of fossil fuels has already been extracted and the supply will be limited in a not too distant future. Sustainable alternatives are therefore essential in order to meet future energy demands.

While there are commercial alternatives already on the market such as solar cells and wind power, a completely new energy infrastructure will be required in the future in order to become completely independent of fossil fuels. One of the most promising alternatives is the *hydrogen economy* [4], where hydrogen serves as energy carrier. The chemical energy stored in hydrogen can be released through reaction with oxygen, where water is the only byproduct in the ideal situation:

$$2H_2 + O_2 \longrightarrow 2H_2O. \tag{1.1}$$

The hydrogen economy can be divided into three main parts: *production*, *storage* and *use*. A chain is not stronger than its weakest link and all these stages have to be optimized in order for hydrogen to become a viable energy source, and at moment none of them have reached the necessary requirements. Hydrogen can be produced by the splitting of water in electrolyzer cells, which ideally are driven by solar power. Other (less sustainable) routes to hydrogen production include separation of hydrogen from various hydrocarbons using chemical reactors and separation membranes, such as steam reforming of methane. The storage of hydrogen is a delicate problem where volume and weight restrictions pose the largest difficulty, especially for mobile applications. Solid storage materials also rely on fast capture and release of hydrogen, which require a fundamental understanding of the different catalytic reactions at play. The final stage, which is to extract the energy for use, is managed by the fuel cell. A fuel cell convert the chemical energy stored in hydrogen to electrical energy and can operate with a higher (theoretical) efficiency compared to combustion and heat engines.

The realization of the hydrogen economy requires a variety of different electrochemical devices that in turn constitute of materials that have to be able to withstand a huge range of external conditions, such as different temperatures, pressures and gaseous environments. Hence, many different types of materials are necessary in order to satisfy these demands. The work in this thesis in focused on solid oxides, a class of materials that can be both good ionic and electronic conductors if subject to high and intermediate temperatures ($> 400\,°\mathrm{C}$). The following section serves as a short introduction to this field and outlines the basic principles of some typical solid oxide devices as well as different relevant materials and their properties. For a more comprehensive review on the subject see, e.g., [5].

1.1 Solid oxide devices

Solid oxide devices, such as electrochemical cells and membranes, generally constitute of three main parts: the *anode*, the *electrolyte* and the *cathode* (see Fig. 1.1). The desired properties of these sub systems depend on the character of the device, which can be designed for many different applications such fuel cells, electrolyzers and chemical reactors, separation membranes and sensors [6, 7]. The electrodes generally need to be catalytically active towards the chemical reactions that takes place at either side of the device and at the same time often required to be mixed ionic-electronic conductors. Electrolytes can be either pure ionic or mixed conductors depending on the device. The former is required for applications where electricity is extracted or supplied through an external circuit that connects the two electrodes, as in fuel cells and electrolyzers.

To demonstrate the working principles of these devices the solid oxide fuel cell [8] will serve as an example (see Fig. 1.1). The fuel cell converts the chemical energy of the reaction in Eq. (1.1) into electricity, which takes place in several steps at the different cell components. The fuel is supplied at the anode where hydrogen adsorbs to the surface and forms protons and electrons, $H_2 \rightarrow 2H^+ + 2e^-$. The oxidant is simultaneously supplied at the cathode side where oxygen is reduced according to $O_2 + 4e^- \rightarrow 2O^{2-}$. The potential across the device then causes ions to diffuse through the electrolyte while electrons travel through an external load and generate electricity. Finally, protons and oxide ions recombine to form water through the reaction $2H^+ + O^{2-} \rightarrow H_2O$. Depending on if the electrolyte is an oxide

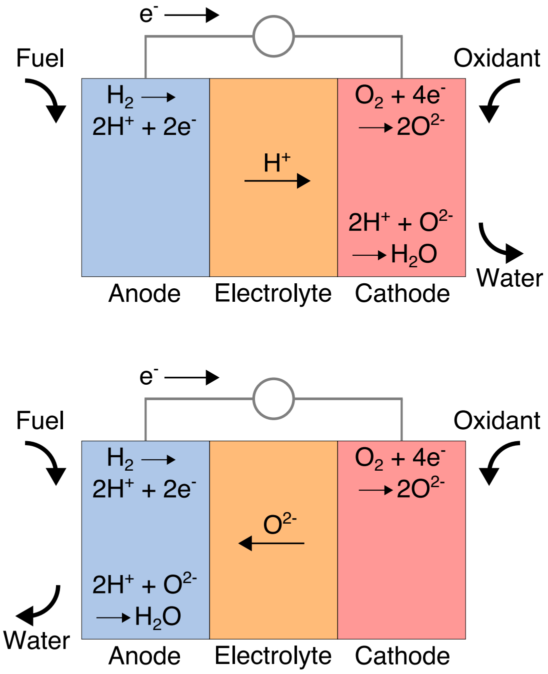

Figure 1.1: The working principle of a proton-conducting (top panel) and an oxide ion-conducting (bottom panel) solid oxide fuel cell.

ion or proton conductor the water will be formed either at the anode or cathode, where the latter is preferred as the former leads to dilution of the fuel.

The workflow of other devices is not that different. Electrolyzers and chemical reactors that produce hydrogen, hydrocarbons or other types of chemicals are basically fuel cells operated in reverse with electricity being supplied to maintain the rate of the considered reactions. For sensors, the cell voltage can be used to probe the concentration of a compound at the anode given that the chemical potential at the cathode is known. For separation membranes, however, there is no external circuit as they rely on mixed-conducting electrolytes where the diffusion is driven by a concentration gradient.

The current technology for these devices is mainly based on oxide ion-conducting electrolytes. The most commonly used materials here are yttria-stabilized zirconia (YSZ) and gadolinium-doped ceria (GDC), which both crystallize in the fluorite structure, as well as strontium and magnesium co-doped $LaGaO_3$, which is a perovskite [9, 10]. YSZ is most widely used but requires high operating temperatures (800-1000 °C). GDC on the other hand exhibit high conductivity at lower temperatures but then also becomes electronically conducting [10].

The rather high temperatures needed for the conventional oxide ion conductors are a bit unpractical since they require long start-up and shut-down times that put the materials under substantial thermal and chemical stress. This have led to a search for materials that operate at intermediate temperatures (400-700 °C) and for this reason has proton-conducting ceramics gained much attention due to the lower activation energy for proton migration [11, 12]. Acceptor-doped perovskites are popular materials for proton-conducting electrolytes, which become proton conducting in wet atmospheres due to hydration of oxygen vacancies, and the most promising materials up to this date are yttrium-doped $BaZrO_3$ and $BaCeO_3$ [12–15]. However, these materials are difficult to fabricate and come with detrimental properties such as high grain boundary resistance and poor stability, which reduce the overall performance and limit the use in practical applications. As a consequence, few commercial devices based on proton-conducting perovskites have seen the light of day even though this class of materials have been around for almost 40 years [16]. It is only in the last few years that more applications have come closer to commercialization [17–19].

So far, we have only discussed specific electrolyte materials. Although the electrolyte is central to the device, the need for efficient electrode materials is equally important. In fact, a recent success in the development of proton-conducting fuel cells is attributed to the fabrication of a $BaZrO_3$-based cathode material [17]. Besides being mixed conductors and catalytically active it is important that the electrodes are compatible with the electrolyte in such that they respond similarly to changes in temperature and pressure. The appropriate choice of anode and cathode materials is therefore to large extent determined by the electrolyte [9]. Many of the common anode and cathode materials have perovskite and fluorite structures. For specific examples see, e.g., [9, 12, 20–22].

To conclude, this section only covers the most basic aspects but it still shows that designing electrochemical devices is a difficult task, which requires tailor-made materials with fine-tuned properties. Extensive research in the past has led to improved fabrication techniques and a deeper understanding of these materials, which have allowed for a more intricate materials design. However, in order to proceed further in this endeavor with practical applications the underlying mechanisms for different properties need to be fully understood, and for this do theory and modeling become an important tool.

1.2 Thesis aim and outline

This thesis addresses several problems related to oxides when used as ionic and electrical conductors. Focus lies on ternary oxides with the perovskite structure although the last paper considers a selection of binary oxides as well. The applied methodology is mainly that of first-principles calculations and thermodynamic modeling.

The major part of the thesis, Papers I-VII, concerns different aspects of acceptor-doped $BaZrO_3$, one of the most prominent proton-conducting perovskites. The first four papers cover an aspect that is arguably the most important for practical applications, namely the formation of space-charges at grain boundaries that limit the total conductivity of polycrystalline samples. The aim here is to understand the mechanism that govern this phenomenon and why these effects are less prominent in similar materials such as acceptor-doped $BaCeO_3$. The second topic is of a more structural character and refers to the chemical expansion that follows from hydration of oxygen vacancy, which causes stress and can reduce the long-term stability of the material. This problem is addressed from a point defect point of view in Paper V where defect formation volumes play an important role. The third and final topic concerns the theoretical description of the oxidation of acceptor-doped perovskites where $BaZrO_3$ serves as a model system. This reaction governs the formation of holes and plays an important part in determining the conductive nature of these materials. Holes are not well described by standard electronic structure methods since these fails to predict accurate band gaps and to fully capture localized electronic states. More advanced theoretical and computational methods have been applied here with the purpose to study to which extent the shortcomings of the standard methods affect the description of holes in these oxides.

The last two papers deal with a novel oxyhydride perovskite and the oxygen vacancy defect, respectively. In Paper VIII the vibrational properties of hydride ions in $BaTiO_{3-x}H_x$ are probed using theoretical calculations and neutron scattering techniques in order to determine the nature of electronic carriers in the material. The final paper, Paper IX, is a study of the general behavior of oxygen vacancies in a large set of oxide hosts with different electronic structures.

The thesis is outlined as follows. Chapter 2 gives a background to the structure and properties of oxides with focus on acceptor-doped perovskites and oxyhydrides. The following two chapters give a theoretical background to defect chemistry, space-charge formation and conductivity. Details regarding the considered computational first-principles methods are presented in Chapter 5. At last, Chapters 6 and 7 give a summary of the results and an outlook for future work.

2

Solid oxide materials

Solid oxides are versatile materials that can be found almost everywhere on earth due the high electronegativity of oxygen together with the abundance of oxygen in air and water. The simplest compounds are binary oxides, which have practical application in many different areas. Many of the conventional solid oxide ion conductors are of this form, such as ZrO_2 and CeO_2 [10]. Another important class of materials are the transparent conducting oxides (TCOs), which are useful for optoelectronic applications and where the most prominent compounds are of binary form: SnO_2, In_2O_3, TiO_2, ZnO, etc. [23]. Some binary oxides are also used as catalysts [24]. One of the most abundant materials on earth is SiO_2, a binary oxide that can crystallize in many different phases and has a widespread use, such as being a wide-band gap insulator for microelectronics as well as being a major constituent of cement, only to name a few [25]. Slightly more complex are ternary compounds where the oxide ion is accompanied by two other elements. An important set of materials among these are oxides with the perovskite structure. The main focus of this thesis lies on perovskite oxides, although some of the binary compounds mentioned above have been considered in Paper IX.

The remainder of this chapter is divided into three sections. Section 2.1 gives a more detailed description of the structure of perovskites in general, while Section 2.2 and 2.3 treat two sub classes within this family of oxides: *proton conductors* and *oxyhydrides*. These last two sections give an introduction to the materials under investigation here and discuss the problems that this thesis sets out to describe and understand.

2.1 The perovskite structure

Perovskite oxides have been of large interest for scientists over the last century since this class of materials exhibits a wide range of physical properties even though the crystal structure is quite simple. These materials have been shown to display properties such as piezoelectricity, pyroelectricity and ferroelectricity [26, 27], proton, ionic and electronic conductivity [14, 28, 29], superconductivity [30–32], ferromagnetism [33], and magnetoresistance [34, 35]. Perovskite oxides are ionic compounds with the general chemical formula ABO_3, where A and B are cations. In their most simple forms the A- and B-site sub lattices are each occupied by only one species but for perovskites with more complex chemical formulas multiple species can be present on each sub lattice.

The perovskite crystal structure comes in many different forms and a few characteristic examples are shown in Fig. 2.1. The archetype is the cubic phase for which the unit cell contains only one ABO_3 formula unit. The A-site is located at the corner of the cell while the B-site resides at the center. The oxygen ions occupy the face centers and form an octahedral unit with the B-site at its center (see Fig. 2.1). Other perovskite structures can be characterized through distortions of the cubic structure where one or several ions are displaced from their cubic lattice sites. For example, a polar distortion where the B-site ion is displaced along one of the main axes leads to a tetragonal phase, which is responsible for ferroelectric properties of these materials. A common type of distortion is the tilting of the oxygen octahedra, which can occur both in and out of phase, along one or several directions. A classification of the various tilts and how they relate to different perovskite phases is described in Ref. [36].

The different perovskite structures and the associated distortions are related to the size of the cations. Assuming that ions are hard spheres with radius r it follows from the cubic perovskite structure that

$$r_A + r_O = \sqrt{2}\,(r_B + r_O)\,. \tag{2.1}$$

The ratio between the left and right hand side of this expression,

$$t = \frac{r_A + r_O}{\sqrt{2}\,(r_B + r_O)}, \tag{2.2}$$

is referred to as *Goldschmidt tolerance factor* [37] and serves as a predictor for different perovskite structures. $t = 1$ yields the condition above and most likely corresponds the cubic phase, while larger and lower values are more prone to result in structures with reduced symmetry. More specifically, for $t < 1$ the A-site cation is too small, which leads to octahedral tilts, while in the case of $t > 1$ the B-site cation is to small and is easily displaced [27]. For very large size mismatches ($t \ll 1$ or $t \gg 1$) it is likely that the oxide will crystallize in a non-perovskite structure.

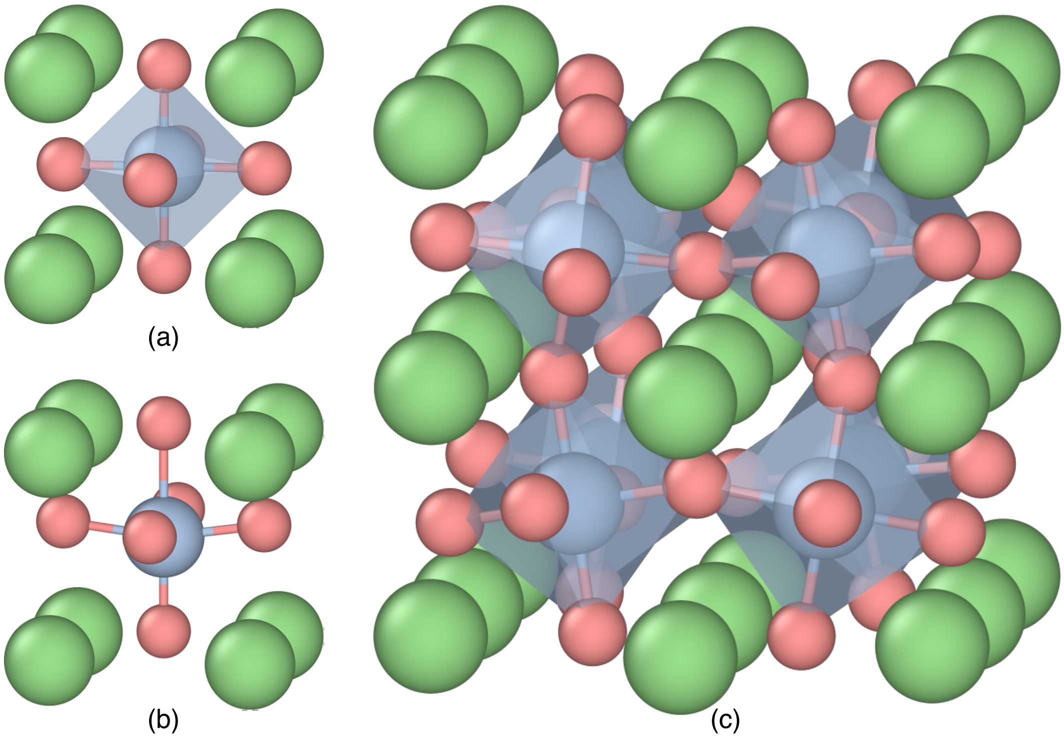

Figure 2.1: A selection of different perovskite structures: (a) cubic, (b) tetragonal with a polar distortion and (c) orthorhombic with octahedral tilting. Green, blue and red atoms represent A, B and oxygen sites, respectively.

2.2 Proton conductors

The earliest evidence of significant proton conductivity in perovskite oxides dates back to a study of acceptor-doped $LaYO_3$ and $SrZrO_3$ in 1980 [16]. During the following two decades many different compounds and acceptor dopants were considered [38–46] and among these acceptor-doped $BaZrO_3$ and $BaCeO_3$ stand out due to their high bulk proton conductivity. While $BaCeO_3$ and other cerates were recognized early on as a promising proton conductors, the initial prospects for $BaZrO_3$ were not as good since this material displayed low total proton conductivity. It was not until the total conductivity could be separated into individual bulk and grain boundary components that it became evident that $BaZrO_3$ displays superior bulk conductivity and that the low conductivity in polycrystalline samples was due to high grain boundary impedance [13, 45]. $BaZrO_3$ and other zirconates are very difficult to sinter and grain boundaries are therefore almost always present in these materials. Grain boundaries in cerates are also resistive but to a lower degree and are thus not as detrimental for the total conductivity. The cerates do, however, suffer from stability issues that severely limits their use in practical applications. For instance, $BaCeO_3$ easily decomposes to form $BaCO_3$ and binary oxides when it comes contact with CO_2 [13]. $BaZrO_3$, on the other hand, displays very high chemical stability and this material has therefore received more attention in recent years, where major efforts have been devoted to understand and reduce the influence of grain boundaries on proton conductivity.

The major part of this thesis is devoted to modeling of different properties of $BaZrO_3$ and the remainder of this section covers two aspects that are especially important for proton conduction in this material, but also for perovskite oxides in general: acceptor doping and the presence of grain boundaries. The former is essential for incorporating protons into the material and latter concerns the overall proton conductivity as discussed above. Together with a short introduction to these subjects the following subsections will try to provide a motivation for the work in Papers I-VII.

2.2.1 Acceptor doping

Many of the pristine perovskites are wide band gap oxides with a low number of intrinsic defects and are thus poor ionic and electronic conductors. Protons in these materials are extrinsic defects that can be incorporated through hydration of doubly charged oxygen vacancies, which is described by the hydration reaction that in Kröger-Vink notation [47] reads as

$$\mathrm{H_2O(g)} + \mathrm{v}_\mathrm{O}^{\bullet\bullet} + \mathrm{O}_\mathrm{O}^{\times} \rightleftharpoons 2\mathrm{OH}_\mathrm{O}^{\bullet}, \tag{2.3}$$

where protons are treated as hydroxide ions. A sufficient amount of charged vacancies have to be created in order to accommodate the number of protons required for adequate proton conductivity in practical applications. This can be accomplished by acceptor doping.

In semiconductor physics doping typically refers to when a defect is introduced in a material that either donates or accepts (binds) electrons to and from the host lattice, where the latter leads to the formation of electron holes. The charge compensation of dopants is, however, not limited to electronic defects and doping can be used to enhance the concentration of charged point defects. acceptor doping in this context refers to substituting a part of the cations with ions of lower valence (here denoted M) and, in turn, doubly charged oxygen vacancies are formed to maintain charge neutrality. The most common scheme for the $BaZrO_3$, $BaCeO_3$ and other $A^{2+}B^{4+}O_3^{2-}$ perovskites is to substitute B^{4+} with M^{3+}, which is described by the reaction

$$2B\mathrm{O_2(s)} + M_2\mathrm{O_3(s)} \longrightarrow 2B_B^{\times} + 2M_B' + 5\mathrm{O}_\mathrm{O}^{\times} + \mathrm{v}_\mathrm{O}^{\bullet\bullet}. \tag{2.4}$$

Many different dopant species have been considered and it has been established that yttrium leads to the best performance for both $BaZrO_3$ and $BaCeO_3$ [15]. While not as widely considered as B-site doping in these materials, A-site acceptor doping with alkali metals has also been proposed [48]. With an increase in the concentration of oxygen vacancies also comes enhanced oxide ion conductivity since oxide ion diffusion is mediated by vacancies (for more details regarding ionic diffusion see Section 4.1). The co-ionic properties (mixed proton-oxide ion conduction) of $BaZr_{0.7}Ce_{0.2}Y_{0.1}O_{3\text{-}\delta}$ was recently utilized in a membrane reactor for methane dehydroaromatization [18].

Associated with the hydration reaction in Eq. (2.3) is a change in volume of material, a *chemical expansion*, which follows from the difference in formation volumes of the involved defects. For large defect concentrations this effect can be quite significant, which puts the material under severe strain that can affect the long-term stability. This phenomenon has been observed experimentally in both $BaZrO_3$ and $BaCeO_3$ [13, 49–51] and is the topic of Paper V.

Instead of creating oxygen vacancies, acceptor doping in perovskites can also lead to the formation of holes. This occurs mainly in oxidizing environments such as the conditions present at cathodes in many electrochemical cells. Yttrium-doped $BaZrO_3$ even becomes predominantly hole conducting at high temperatures and high oxygen partial pressures [52–54]. The two different doping scenarios are related through the oxidation reaction

$$\frac{1}{2}\mathrm{O_2(g)} + \mathrm{v}_\mathrm{O}^{\bullet\bullet} \rightleftharpoons 2\mathrm{h}^{\bullet} + \mathrm{O}_\mathrm{O}^{\times}, \tag{2.5}$$

which describes the formation of two holes at the expense of a doubly charged oxygen vacancy. Modeling of this process is a delicate problem since holes are involved and the character of the reaction has been predicted as both exothermic and endothermic. An accurate description of the reaction relies on a proper treatment of the electronic structure. This especially concerns the band gap and localized states, which are usually not well described by standard electronic structure methods. It is therefore necessary to consider more elaborate approaches and this issue is addressed in Papers VI and VII.

2.2.2 Grain boundaries

A crystalline material is to a large extent described by its lattice structure. In principle, this periodic arrangement of atoms can extend throughout the whole material forming a single crystal, but in practice this is often not the case. Many materials are usually polycrystalline with a microstructure constituting of grains, where each grain is a single crystal. At the interface between two grains there is a mismatch in the crystal structure, giving rise to a planar defect along the interface,

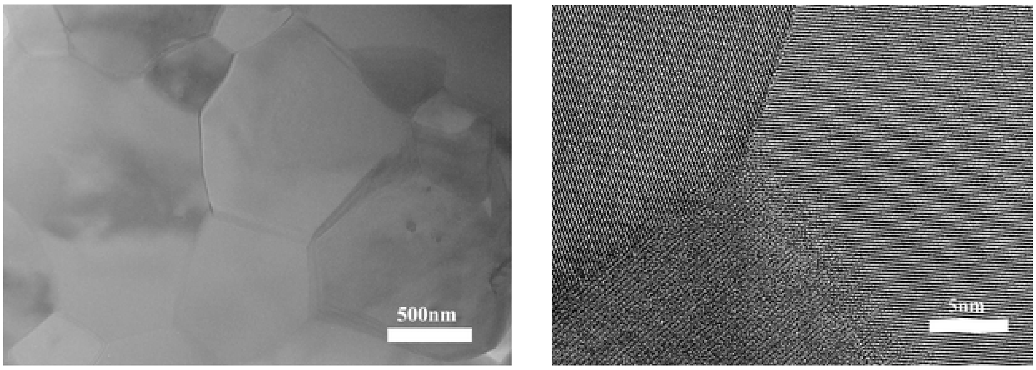

(a) TEM image of individual grains. (b) HRTEM image of grain boundaries.

Figure 2.2: TEM images of the microstructure of $BaZr_{0.95}Y_{0.05}O_{2.975}$ [56].

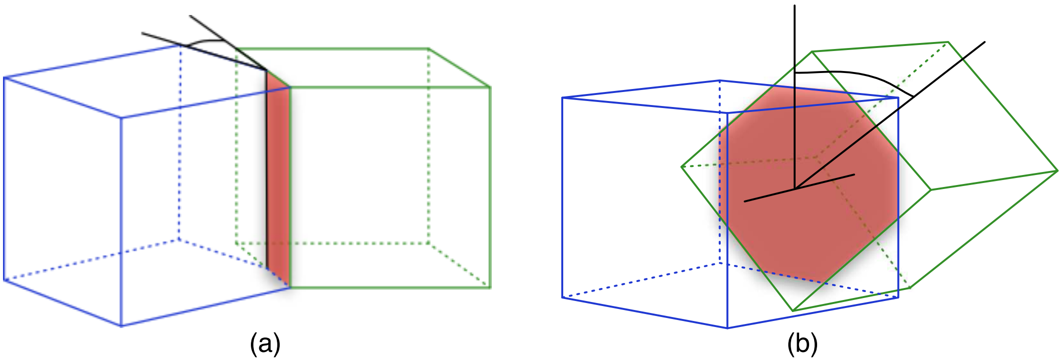

Figure 2.3: Schematic representation of a (a) tilt and (b) twist grain boundary, where the red shaded regions correspond to the grain boundary plane.

which is referred to as a grain boundary. Grain boundaries often exhibit different properties compared to the grain interior since the structure and possibly also the stoichiometry of the grain boundary is different, which is the case in many oxides where these interfaces are the source of various exotic ionic and electronic properties [55]. The size and morphology of grains in a material depend on sinterability, fabrication methods and external conditions (temperature, pressure, etc.). As an example the microstructure of $BaZr_{0.95}Y_{0.05}O_{2.975}$ is shown in Fig. 2.2, where the structure is dense with well-defined grains and grain boundaries.

Grain boundaries come in many different shapes depending on grain orientation. To understand grain boundary structures it is convenient to start with a single crystal that is split in half to form two smaller crystals (or grains). A grain boundary can then be obtained by rotating one of the grains relative to the other. A *tilt*

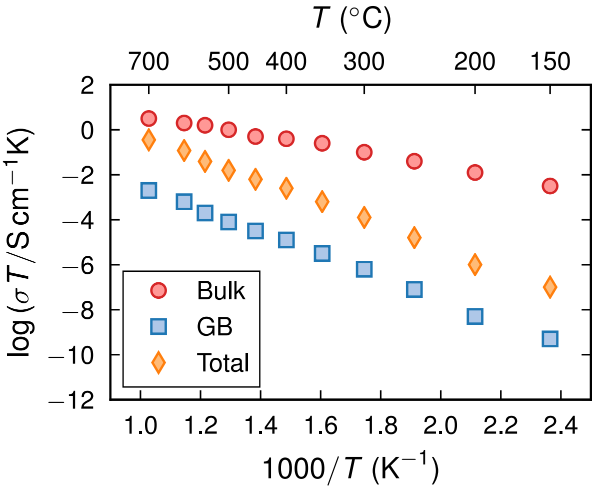

Figure 2.4: Total, bulk and grain boundary proton conductivity of $BaZr_{0.94}Y_{0.06}O_{3-\delta}$. Bulk and grain boundary conductivities are taken from [59]. The total conductivity is calculated based on the bulk and grain boundary contributions using a grain size of 1 µm.

boundary is formed if the rotation occurs around an axis parallel to the interface while a *twist boundary* is the result of a rotation around the axis that is perpendicular to the interface (see Fig. 2.3). Grain boundaries in real materials generally contain both twist and tilt components.

As already pointed out in the introduction and in the beginning of this section, the great interest in grain boundaries in acceptor-doped $BaZrO_3$ lies in the fact that they display high proton resistance [13, 52, 57–59]. To demonstrate the effect of this phenomenon a study of $BaZr_{0.94}Y_{0.06}O_{3-\delta}$ [59] serves as an example (see Fig. 2.4). The conductivity was found to be several orders of magnitude lower at the grain boundaries compared to the bulk and the difference becomes more pronounced at lower temperatures. The low conductivity at boundaries determines the rate and as a consequence the total conductivity becomes lower than the bulk conductivity.

It has been concluded that the low grain boundary conductivity in $BaZrO_3$ is an intrinsic property as the grain boundaries are free of secondary phases (see Fig. 2.2) [56, 60–62]. At present there are two known factors that can explain the high grain boundary resistance, where one is more related to the proton mobility while the other concern the proton concentration. The structural disorder at the boundaries lead to changes in interatomic distances that can increase the migration barrier for proton diffusion and reduce the mobility. First-principles studies of proton migration in grain boundaries have indeed shown that migration barriers can be larger at the grain boundary interface in $BaZrO_3$ [63, 64] as well as in $BaCeO_3$ [65].

The other factor that influences the grain boundary conductivity is the presence of space-charges at the grain boundaries. The space-charge formation follows from that positively charged defects accumulate at the grain boundary and give rise to an electrostatic potential. In turn, the potential depletes the surrounding regions (the space-charge layers) of charge carriers and the conductivity is reduced. There is both experimental [56, 59, 62, 66–71] and theoretical [72–76] evidence for space-charge formation at grain boundaries in $BaZrO_3$, where the latter includes the work in Papers I-IV. Space-charge formation at grain boundaries has also been seen in other perovskites, such as $SrTiO_3$ [77], $SrZrO_3$ [78] and $LaGaO_3$ [79], as well as in other oxide materials, such as acceptor-doped CeO_2 and ZrO_2 [80]. The formation of space-charges is not limited to grain boundaries and several studies have addressed space-charge effects at surfaces and other interfaces in $BaZrO_3$ [81–84].

Several different schemes to reduce the grain boundary resistance can be found in the literature. A common approach that has been proven to be quite successful is the substitution of some amounts of zirconium with cerium to form a $BaZrO_3$-$BaCeO_3$ solid solution such as $BaZr_{0.7}Ce_{0.2}Y_{0.1}O_{3\text{-}\delta}$, a compromise that leads to improved conductivity but only a moderate loss in stability [13, 17, 18, 85]. Much attention has been directed towards different sintering techniques where the use various sintering aids such as zinc and nickel have been shown to improve grain growth, which leads to increased grain sizes and consequently to a reduction in the grain boundary density [86, 87]. High temperature annealing has been shown to improve the grain boundary conductivity [88], which has been attributed to the segregation of acceptor dopants to the grain boundary cores [69, 89], an aspect that was consider in Paper III. Furthermore, in a very recent publication it was reported that grain boundary resistances could be eliminated altogether by considering a columnar structure for the $BaZr_{0.85}Y_{0.15}O_{3-\delta}$ electrolyte in a fuel cell device [90].

2.3 Oxyhydrides

In more recent years, it has been demonstrated that hydrogen can also be incorporated into perovskite oxides as hydride ions, forming an oxyhydride phase. While the first discovery dealt with the more exotic perovskite-like material $LaSrCoO_3H_{0.7}$ [91], more recent results concern conventional Ti-based perovskites with the chemical formula $A\mathrm{TiO}_{3-x}\mathrm{H}_x$, where A = (Ca, Sr, Ba) [92, 93]. These materials are mixed conductors, displaying both hydride and electronic conductivity [94]. Among these three compounds $BaTiO_{3-x}H_x$ stands out due its ability to incorporate a large amount of hydrogen, where as much as $x = 0.6$ has been reported [92]. It also displays intriguing electrical properties by going from a semiconducting to a metallic state with increasing hydride concentration in epitaxial thin films, unlike for the

Ca- and Sr-based counterparts where only a metallic state is observed [95]. Up until now most studies on these materials are fundamental in nature with focus on understanding the materials properties, however, potential applications could be various electrochemical devices. It has also been demonstrated that these oxyhydrides can act as precursors for other exotic materials, such as oxynitrides [96].

The $A\mathrm{TiO}_{3-x}\mathrm{H}_x$ oxyhydrides are formed under extremely reducing conditions, using a reduction agent such CaH_2:

$$\mathrm{CaH_2(s)} + \mathrm{O}_\mathrm{O}^\times \rightleftharpoons \mathrm{CaO(s)} + \frac{1}{2}\mathrm{H_2(g)} + \mathrm{H}_\mathrm{O}^\bullet + \mathrm{e}'. \tag{2.6}$$

Under reducing conditions these materials also contain oxygen vacancies and a competing reaction is thus

$$\mathrm{O}_\mathrm{O}^\times \rightleftharpoons \frac{1}{2}\mathrm{O_2(g)} + \mathrm{v}_\mathrm{O}^{\bullet\bullet} + 2\mathrm{e}'. \tag{2.7}$$

Unlike many other oxyhydrides, these perovskite materials are stable in air up to temperatures of about 400 °C, where hydrogen starts to leave the materials.

Despite the increased interest in these systems in the recent years many fundamental questions still remain, especially those concerning the hydride diffusion mechanisms. This is an ongoing discussion and several different explanations have been proposed in the literature, which include interstitial hydride diffusion as well as migration mediated by oxygen vacancies [97–99]. It is also not clear if there is a coupling between the hydride and electron dynamics, and an important results within this context is the recent discovery of an oxyhydride that displays hydride conductivity but at the same time is an electrical insulator [100, 101]. The contribution from this thesis in the context of oxyhydrides is the work of Paper VIII, where the character of the electronic carriers in $\mathrm{BaTiO}_{3-x}\mathrm{H}_x$ is studied by the means of theoretical calculations aided by neutron scattering experiments. More specifically, the question we try to answer is whether the excess electron can be described as a band state, which is associated with the Ti ions being in mixed +3/+4 valence state, or if the electron localizes as small polaron to form a single local Ti^{3+} ion on the Ti^{4+} sub lattice.

3

Thermodynamics of point and planar defects

In theory, crystalline materials can be described by a perfect infinite structure of repeated primitive cells. This is never the case in reality since defects, which break the symmetry of the perfect lattice, will always be present in materials at finite temperatures. There exist a large number of different defect types and they determine many materials properties. Defects are a central part in all the appended papers in this thesis and most of the work done here can be described as the interplay between defects and the crystal structure.

Defects can be categorized based on their extension in space. Those with lowest dimensionality correspond to irregularities in the structure associated with single atoms and ions and these are referred to as point defects. There exist several different types of point defects, where a few characteristic ones are depicted in Fig. 3.1. A *vacancy* is a lattice site without an atom and an *interstitial* defect is an atom that is not located at a lattice site. A *substitutional* defect refers to when the atom located at a lattice site is not the original one of the ideal lattice. Interstitial and substitutional defects can be further classified as either *intrinsic* or *extrinsic* depending on if the origin of the involved atom is of native or foreign character with respect to the host material. Point defects can also trap electrons and holes and many defects also carry a net charge. Defects of higher spatial dimension include line (1D), planar (2D) and bulk (3D) defects.

The purpose with this chapter is to present a theoretical framework for thermodynamic modeling of point defects that can be used to relate microscopic and macroscopic properties. Planar defects are also covered to some extent where the emphasis is on grain boundaries. The chapter is organized in the following way. Sections 3.1-3.4 cover different aspects of point defect formation in bulk systems.

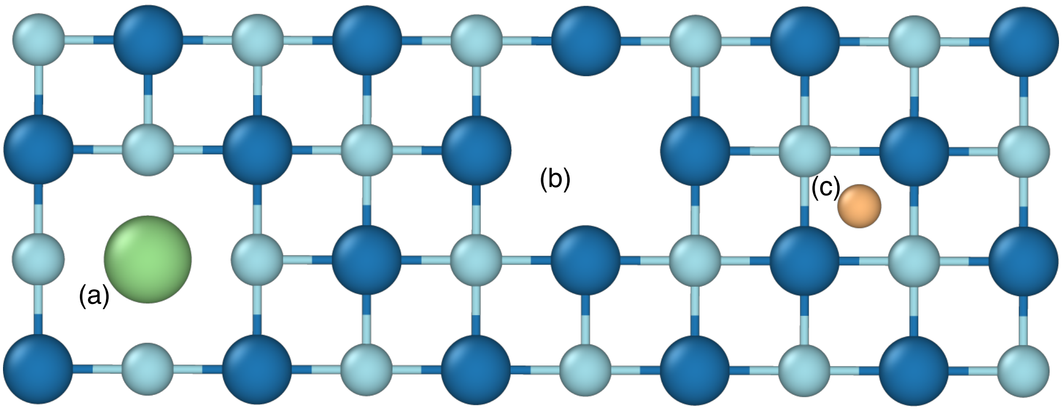

Figure 3.1: Schematic representation of point defects in a crystal lattice. Three defects are present: (a) a substitutional defect, (b) a vacancy, and (c) an interstitial defect.

Grain boundaries are then introduced in Section 3.5. The last section gives a theoretical description of space-charge formation, which is a consequence of point defect accumulation at grain boundaries and other interfaces.

3.1 Chemical equilibrium

The formation of point defects is associated with a change in the Gibbs free energy that can be written as

$$\Delta G = \Delta H - T\Delta S, \tag{3.1}$$

where ΔH and ΔS are changes in the enthalpy and entropy, respectively, and T is temperature. It is convenient to further separate the configurational part of the entropy, ΔS^{conf}, from the other entropic contributions according to

$$\Delta S = \Delta S^{\text{else}} + \Delta S^{\text{conf}}. \tag{3.2}$$

An important approximation will now be made that simplifies the treatment of point defects significantly: defects do *not* interact with each other. While it is fairly obvious that this is valid at very low defect concentrations, a scenario which is often referred to as the *dilute limit*, this assumption has been shown to be reasonable even when defects accumulate in larger numbers. It should be noted that it is still possible to treat defect-defect interactions to some extent within approximation. For instance, two neighboring defects that form a pair can be treated as a single non-interacting defect species. Certain explicit interactions can also be introduced later on in a rather simple manner, which is shown further on in Section 3.6.

A general expression can now be derived that relates the equilibrium concentration of a defect to the corresponding defect formation energy by using Eq. (3.1) as a starting point. The premise here is that n non-interacting defects of an arbitrary species are formed on a discrete lattice with N sites, where both N and n are large numbers and $N > n$. Eq. (3.1) can then be written as

$$\Delta G = n\Delta H^{\mathrm{f}}_{\mathrm{def}} - Tn\Delta S^{\mathrm{f}}_{\mathrm{def}} - T\Delta S^{\mathrm{conf}} = n\Delta G^{\mathrm{f}}_{\mathrm{def}} - T\Delta S^{\mathrm{conf}}, \tag{3.3}$$

where $\Delta H^{\mathrm{f}}_{\mathrm{def}}$ and $\Delta S^{\mathrm{f}}_{\mathrm{def}}$ is the change in enthalpy and entropy (not including configurational entropy) upon formation of a single defect, and $\Delta G^{\mathrm{f}}_{\mathrm{def}} = \Delta H^{\mathrm{f}}_{\mathrm{def}} - T\Delta S^{\mathrm{f}}_{\mathrm{def}}$ is the corresponding change in free energy. The configurational part of the entropy can be expressed as

$$\Delta S^{\mathrm{conf}} = k \ln \Omega, \tag{3.4}$$

where k is Boltzmann's constant and Ω is the multiplicity. The latter corresponds the number of possible ways to distribute the defects on the lattice and is for this scenario given by

$$\Omega = \frac{N!}{n!\,(N-n)!}. \tag{3.5}$$

By making use of Stirling's approximation ($\ln x! \approx x \ln x - x$ for $x \gg 1$) the configurational entropy can be written as

$$\Delta S^{\mathrm{conf}} = k \left(N \ln \frac{N}{N-n} - n \ln \frac{n}{N-n} \right) \tag{3.6}$$

and it then follows that total change in free energy can be expressed as

$$\Delta G = n\Delta G^{\mathrm{f}}_{\mathrm{def}} - kT \left(N \ln \frac{N}{N-n} - n \ln \frac{n}{N-n} \right). \tag{3.7}$$

The total free energy of the defective system can be written as $G_{\mathrm{def}} = G_0 + \Delta G$, where G_0 is the free energy of the pristine material. In equilibrium, G_{def} should be minimized with respect to n and since G_0 is independent of n this corresponds to

$$0 = \frac{\mathrm{d}G_{\mathrm{def}}}{\mathrm{d}n} = \frac{\mathrm{d}}{\mathrm{d}n} \left(\Delta G \right) = \Delta G^{\mathrm{f}}_{\mathrm{def}} + kT \ln \frac{n}{N-n}. \tag{3.8}$$

At this point it is suitable to introduce the defect concentration c. By replacing n with c and N with the maximum concentration c^{max}, Eq. (3.8) can be written as

$$0 = \Delta G^{\mathrm{f}}_{\mathrm{def}} + kT \ln \frac{c}{c^{\mathrm{max}} - c} \tag{3.9}$$

and the equilibrium concentration is thus given by

$$c = c^{\mathrm{max}} \frac{1}{1 + \exp\left(\Delta G^{\mathrm{f}}_{\mathrm{def}}/kT \right)}. \tag{3.10}$$

In the dilute limit $c \ll c^{\mathrm{max}}$ and Eq. (3.10) reduces to the more simple expression

$$c = c^{\mathrm{max}} \exp\left(-\frac{\Delta G^{\mathrm{f}}_{\mathrm{def}}}{kT} \right). \tag{3.11}$$

3.2 Law of mass action

The previous section showed that configurational entropy is a major driving force for point defect formation. This is, however, not the only mechanism and defect formation is often influenced by interactions. In a real material there are typically many different types of point defects, which can interact with each other and the environment.

The energy associated with the addition or removal of a particle i in a certain environment is given by the chemical potential, which is defined as

$$\mu_i = \left(\frac{\partial G}{\partial n_i}\right)_{T,P,n_{j\neq i}}. \tag{3.12}$$

With the same approach as in the previous section concerning the configurational entropy the chemical potential in a crystalline material can derived:

$$\mu_i = \mu_i^\circ + kT \ln \frac{c_i}{c_i^{\max} - c_i}, \tag{3.13}$$

where μ_i° is the chemical potential in a reference state. In the dilute limit this reduces to

$$\mu_i = \mu_i^\circ + kT \ln \frac{c_i}{c_i^{\max}}. \tag{3.14}$$

A similar expression is obtained for the chemical potential of the constituents of an ideal gas:

$$\mu_i = \mu_i^\circ + kT \ln \frac{p_i}{p^\circ}, \tag{3.15}$$

where p_i is the partial pressure and p° is the reference pressure.

Consider now the chemical reaction

$$n_\mathrm{A}\mathrm{A} + n_\mathrm{B}\mathrm{B} \rightleftharpoons n_\mathrm{C}\mathrm{C} + n_\mathrm{D}\mathrm{D}, \tag{3.16}$$

where n_A, n_B, n_C, and n_D denote the number of species A, B, C, and D that takes part in the reaction. In equilibrium the free energy of the reactants (A and B) is equal to that of the products (C and D), which corresponds to

$$n_\mathrm{A}\mu_\mathrm{A} + n_\mathrm{B}\mu_\mathrm{B} = n_\mathrm{C}\mu_\mathrm{C} + n_\mathrm{D}\mu_\mathrm{D}. \tag{3.17}$$

Substituting μ_i in this expression with Eq. (3.14) followed by some algebra lead to the *law of mass action*:

$$\frac{c_\mathrm{C}^{n_\mathrm{C}} c_\mathrm{D}^{n_\mathrm{D}}}{c_\mathrm{A}^{n_\mathrm{A}} c_\mathrm{B}^{n_\mathrm{B}}} = \exp\left(-\frac{\Delta G^\circ}{kT}\right) \equiv K, \tag{3.18}$$

where $\Delta G^\circ = n_C\mu_C^\circ + n_D\mu_D^\circ - n_A\mu_A^\circ - n_B\mu_B^\circ$ and K is the equilibrium constant.

With the mass action law it is possible to obtain equilibrium concentrations of the involved species for any given reaction. A simple example for a reaction in oxides is the intrinsic reduction reaction in Eq. (2.7), for which the equilibrium constant is given by

$$K_{\mathrm{red}} = c_{\mathrm{v}} n_{\mathrm{e}}^2 p_{\mathrm{O}_2}^{1/2} c_{\mathrm{O}}^{-1}, \tag{3.19}$$

where c_{v}, n_{e} and c_{O} is the oxygen vacancy, electron, and oxygen concentration, respectively, and p_{O_2} is the oxygen partial pressure. Assuming that no other charged defects are present, the charge neutrality condition is given by $2c_{\mathrm{v}} = n_{\mathrm{e}}$. Site restriction on the oxygen sub lattice gives $c_{\mathrm{v}} + c_{\mathrm{O}} = N_{\mathrm{O}}$, where N_{O} is the concentration of oxygen sites. For small concentrations is $c_{\mathrm{v}} \ll N_{\mathrm{O}}$ and it follows that $c_{\mathrm{O}} \approx N_{\mathrm{O}}$. With these conditions the electron and oxygen vacancy concentrations can be written as

$$n_{\mathrm{e}} = 2c_{\mathrm{v}} = \left(2N_{\mathrm{O}}K_{\mathrm{red}}\right)^{1/3} p_{\mathrm{O}_2}^{-1/6}. \tag{3.20}$$

More involved examples are the oxidation and hydration of oxygen vacancies in acceptor-doped perovskites. These materials contain doubly charged oxygen vacancies, which are formed to compensate the negatively charged acceptor dopants. The vacancies can then be either hydrated or oxidized depending on the environmental conditions, which is described in more detail in Section 2.2. The equilibrium constant of the oxidation reaction in Eq. (2.5) is given by

$$K_{\mathrm{ox}} = \frac{c_{\mathrm{O}} n_{\mathrm{h}}^2}{c_{\mathrm{v}} p_{\mathrm{O}_2}^{1/2}}, \tag{3.21}$$

where n_{h} is the hole concentration. The site restriction is the same as in the previous example but c_{v} is no longer negligible since it is of the same order as the dopant concentration c_{A}, which is often quite large. The charge neutrality condition is given by $2c_{\mathrm{v}} + n_{\mathrm{h}} = c_{\mathrm{A}}$. Typically only a small fraction of the vacancies become oxidized ($n_{\mathrm{h}} \ll c_{\mathrm{v}}$) and the charge neutrality condition simplifies to $2c_{\mathrm{v}} \approx c_{\mathrm{A}}$. Based on these conditions the hole concentration can be written as

$$n_{\mathrm{h}} = \left(\frac{c_{\mathrm{A}}K_{\mathrm{ox}}}{2N_{\mathrm{O}} - c_{\mathrm{A}}}\right)^{1/2} p_{\mathrm{O}_2}^{1/4}. \tag{3.22}$$

For the hydration reaction in Eq. (2.3) the equilibrium constant is given by

$$K_{\mathrm{hydr}} = \frac{c_{\mathrm{OH}}^2}{c_{\mathrm{v}} c_{\mathrm{O}} p_{\mathrm{H_2O}}}. \tag{3.23}$$

Site restriction now also includes the proton concentration c_{OH} and is given by $c_{\mathrm{OH}} + c_{\mathrm{v}} + c_{\mathrm{O}} = N_{\mathrm{O}}$, where the corresponding charge neutrality condition reads as

$2c_\mathrm{v} + c_\mathrm{OH} = c_\mathrm{A}$. The proton concentration can then be written as

$$c_\mathrm{OH} = N_\mathrm{O} \frac{p_{\mathrm{H_2O}} K_\mathrm{hydr}}{p_{\mathrm{H_2O}} K_\mathrm{hydr} - 4} \left[1 - \sqrt{1 - \frac{p_{\mathrm{H_2O}} K_\mathrm{hydr} - 4}{p_{\mathrm{H_2O}} K_\mathrm{hydr}} \cdot \frac{c_\mathrm{A}}{N_\mathrm{O}} \left(2 - \frac{c_\mathrm{A}}{N_\mathrm{O}} \right)} \right]. \tag{3.24}$$

3.3 Electrons and holes

So far have electrons and holes been treated in the same way as point defects within the mass action approach. Although the derived expressions for electron and hole concentrations in the previous section [Eq. (3.20) and Eq. (3.22)] are valid for the corresponding reactions, the general expression in Eq. (3.10) is not. Instead, the concentrations of electrons in the conduction band and hole in the valence band are given by

$$n_\mathrm{e} = \int_{\epsilon_\mathrm{CBM}}^{\infty} g(\epsilon) n_\mathrm{FD}(\epsilon) \mathrm{d}\epsilon \tag{3.25}$$

$$n_\mathrm{h} = \int_{-\infty}^{\epsilon_\mathrm{VBM}} g(\epsilon) \left[1 - n_\mathrm{FD}(\epsilon) \right] \mathrm{d}\epsilon, \tag{3.26}$$

where ϵ_VBM and ϵ_CBM is the energy at the valence band maximum (VBM) and conduction band minimum (CBM), respectively, and $g(\epsilon)$ is the density of states. The Fermi–Dirac distribution $n_\mathrm{FD}(\epsilon)$ is given by

$$n_\mathrm{FD}(\epsilon) = \frac{1}{\exp\left[(\epsilon - \mu_\mathrm{e}) / kT \right] + 1}, \tag{3.27}$$

where μ_e is the electron chemical potential.

The integrals in Eq. (3.25) and Eq. (3.26) can in general not be carried our analytically due to the complicated expressions for $n_\mathrm{FD}(\epsilon)$ and in particular $g(\epsilon)$. However, if the electron chemical potential is located well within the band gap with respect to kT then two approximations can be made that simplifies the evaluation of the integrals. First, under this condition the Fermi–Dirac distribution is replaced by the Boltzmann distribution

$$n_\mathrm{FD}(\epsilon) \approx \exp\left(-\frac{\epsilon - \mu_\mathrm{e}}{kT} \right) \tag{3.28}$$

and a similar expression is obtained for the $\left[1 - n_\mathrm{FD}(\epsilon)\right]$-term in Eq. (3.26). Second, only the density of states close to the CBM (VBM) is of relevance here for electrons (holes) due to the exponential form of the distribution, and under such circumstances it is possible to derive analytic expressions for $g(\epsilon)$. With these two simplifications the integrals can be solved analytically (for more details see, e.g., [102]) and the solutions are

$$n_\mathrm{e} = 2\left(\frac{2\pi m_\mathrm{e} kT}{h^2}\right)^{3/2} \exp\left(-\frac{\mu_\mathrm{e} - \epsilon_\mathrm{VBM}}{kT}\right) = N_\mathrm{e} \exp\left(-\frac{\mu_\mathrm{e} - \epsilon_\mathrm{VBM}}{kT}\right) \tag{3.29}$$

$$n_\mathrm{h} = 2\left(\frac{2\pi m_\mathrm{h} kT}{h^2}\right)^{3/2} \exp\left(-\frac{\epsilon_\mathrm{CBM} - \mu_\mathrm{e}}{kT}\right) = N_\mathrm{h} \exp\left(-\frac{\epsilon_\mathrm{CBM} - \mu_\mathrm{e}}{kT}\right), \tag{3.30}$$

where m_e and m_h are the effective mass of electrons and holes, respectively, and h is the Planck constant. Note that these expressions are similar to Eq. (3.11).

In the treatment so far, electrons and holes have been modeled as delocalized band states that extend throughout the crystal. In ionic crystals and polar semiconductors it is also possible for electrons and holes to interact with the lattice and localize within a confined region in space. The combined entity that is the localized charge and the lattice distortion can be treated as a quasiparticle and is referred to as a *polaron*. A polaron is characterized by its size and a distinction is made between *large* and *small* polarons, which are also termed Frölich [103] and Holstein [104] polarons, respectively. The size of a small polaron is on the order of the lattice spacing while large polarons are much larger, typically 10-100 Å [105]. Polarons can be further categorized as either self-trapped (free) or bound, where the former is an electron or hole that localize in the ideal lattice while the latter refers to when the polaronic distortion is mediated by a defect (see Fig. 3.2). For small polarons yet another distinction can be made between localization on an atom or a bond.

If polaron formation is favorable or not is determined by the trapping energy, which is the energy difference between the polaronic state and the band state

$$\Delta G^\mathrm{f}_\mathrm{pol} = G_\mathrm{pol} - G_\mathrm{band}. \tag{3.31}$$

This energy can separated into two contributions: a strain energy that is associated with the lattice distortion and an electrostatic energy arising from the Coulomb interaction between the localized charge and the surrounding ions. The polaronic configuration becomes stable if the unfavorable strain is more than compensated by the electrostatic interactions, which corresponds to $\Delta G^\mathrm{f}_\mathrm{pol} < 0$.

In contrast to band state electrons and holes, small polarons can be seen as a point defects and can be treated within the same thermodynamic formalism. For instance, self-trapped holes in perovskite oxides with a valence band that derives from oxygen p-orbitals can be seen as positively charged oxygen ion defect $\mathrm{O}_\mathrm{O}^\bullet$. It is then appropriate to describe reactions involving holes (and electrons) accordingly such as the oxidation reaction in Eq. (2.5), which then becomes

$$\frac{1}{2}\mathrm{O}_2(\mathrm{g}) + \mathrm{v}_\mathrm{O}^{\bullet\bullet} + \mathrm{O}_\mathrm{O}^\times \rightleftharpoons 2\mathrm{O}_\mathrm{O}^\bullet. \tag{3.32}$$

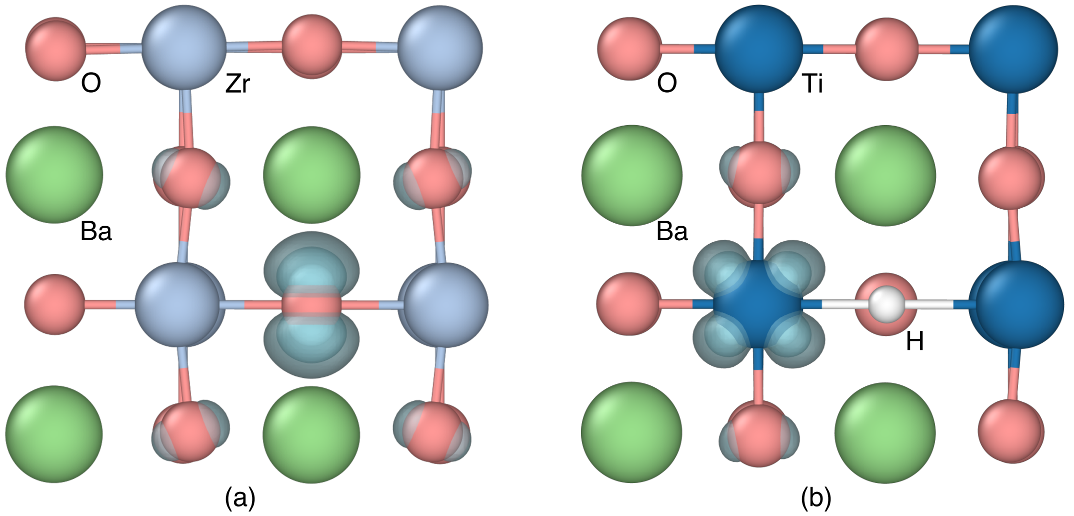

Figure 3.2: Two examples of small polarons in perovskite oxides. (a) Self-trapped hole polaron in $BaZrO_3$ where the hole is localized on an oxygen ion ($O_O^\times + h^\bullet \rightarrow O_O^\bullet$). (b) Bound electron polaron in $BaTiO_{3-x}H_x$ where the electron is localized on a titanium ion and stabilized by a hydride ion [$Ti_{Ti}^\times + e' + H_O^\bullet \rightarrow (Ti_{Ti}'\text{–}H_O^\bullet)^\times$].

3.4 Free energy of defect formation

The key quantity within this thermodynamic treatment is the defect formation energy $\Delta G^{\mathrm{f}}_{\mathrm{def}}$. Several different factors contribute to it and this section provides a short summary these contributions. More practical details of calculating formation energies depend on the applied method and further details on how to determine this quantity using density-functional theory calculations is provided in Section 5.3.

As defined in Eq. (3.3), the free energy of defect formation is given by $\Delta G^{\mathrm{f}}_{\mathrm{def}} = \Delta H^{\mathrm{f}}_{\mathrm{def}} - T\Delta S^{\mathrm{f}}_{\mathrm{def}}$ and it is important to remember that $\Delta S^{\mathrm{f}}_{\mathrm{def}}$ does not include the configurational entropy contribution. More explicitly, the formation energy for a defect in charge state q can be written as

$$\Delta G^{\mathrm{f}}_{\mathrm{def}} = G_{\mathrm{def}} - G_0 - \sum_i \Delta n_i \mu_i + q\mu_{\mathrm{e}}, \tag{3.33}$$

where Δn_i denote the change in atomic species i upon defect formation.

It also possible to express G in terms of the thermodynamic potential $F = U - TS$ (Helmholtz free energy) according to

$$G = H - TS = U + PV - TS = F + PV, \tag{3.34}$$

where U is internal energy, P is pressure and V is volume. The formation energy can then be expressed as

$$\Delta G^{\mathrm{f}}_{\mathrm{def}} = \Delta F^{\mathrm{f}}_{\mathrm{def}} + P\Delta V^{\mathrm{f}}_{\mathrm{def}} = F_{\mathrm{def}} - F_0 - \sum_i \Delta n_i \mu_i + q\mu_{\mathrm{e}} + P(V_{\mathrm{def}} - V_0), \tag{3.35}$$

where $\Delta V^{\mathrm{f}}_{\mathrm{def}} = V_{\mathrm{def}} - V_0$ is the defect formation volume. For solids the PV-term is usually quite small compared to F and can often be neglected, which leads to $G \approx F$ and consequently $\Delta G^{\mathrm{f}}_{\mathrm{def}} \approx \Delta F^{\mathrm{f}}_{\mathrm{def}}$. Furthermore, the vibrational contribution to F usually dominates in the solid phase and a reasonable approximation is therefore

$$G(T) \approx E + F^{\mathrm{vib}}(T), \tag{3.36}$$

where E is the energy at zero Kelvin excluding the zero-point energy.

Within the harmonic approximation (see Section 5.4.1) the vibrational free energy is given by

$$F^{\mathrm{vib}}(T) = \sum_{\boldsymbol{q}s} \left\{ \frac{\hbar\omega_{\boldsymbol{q}s}}{2} + kT \ln \left[1 - \exp\left(-\frac{\hbar\omega_{\boldsymbol{q}s}}{kT} \right) \right] \right\}, \tag{3.37}$$

where $\omega_{\boldsymbol{q}s}$ is the vibrational frequency of the mode with band index s and wave vector $\boldsymbol{q}$. The first term in the sum corresponds to the zero-point contribution. For the vibrational entropy S^{vib}, which relates to F^{vib} as $S^{\mathrm{vib}} = -(\mathrm{d}F^{\mathrm{vib}}/\mathrm{d}T)$, it is important to distinguish between *constant volume* and *constant pressure* conditions, where the latter is usually the scenario of interest while former is often considered in the actual calculation. The difference between the two can be quite significant, as in the case for the oxygen vacancy in $\mathrm{BaZrO_3}$ [106]. It can be shown [106, 107] that the difference between the two entropies is proportional to the formation volume

$$(S^{\mathrm{vib}})_P - (S^{\mathrm{vib}})_V = \alpha_P B_T \Delta V^{\mathrm{f}}_{\mathrm{def}}, \tag{3.38}$$

where α_P is the isobaric thermal expansion coefficient and B_T is the isothermal bulk modulus.

The treatment of the chemical potentials μ_i depends on the physical nature of the reservoirs. For a solid phase the same considerations that was discussed above concerning the approximation $G \approx F$ holds. For the gas phase the free energy follows a quite simple temperature and pressure dependence if the gas can be considered to be ideal. The chemical potential can then be written as

$$\mu(T,p) = \mu_i^{\circ}(T) + kT \ln \frac{p}{p^{\circ}}. \tag{3.39}$$

Furthermore, the chemical potential at the reference pressure can more explicitly be written as $\mu_i^{\circ}(T) = h^{\circ}(T) - Ts^{\circ}(T)$, where the reference enthalpy and entropy for most gases can be readily extracted from thermodynamic tables.

The electron chemical potential μ_e is determined by the charge neutrality condition, which states that the sum of all charges in the material should be equal to zero:

$$\sum_i q_i c_i(\mu_\mathrm{e}) + n_\mathrm{h}(\mu_\mathrm{e}) - n_\mathrm{e}(\mu_\mathrm{e}) = 0. \tag{3.40}$$

This equation can in general only be solved for μ_e numerically since there are often many different types defects present. However, in simple cases such as the reactions considered in Section 3.2 it is possible to find analytic expressions for μ_e.

3.5 Grain boundary formation and defect segregation

Unlike for point defects, the formation of grain boundaries is usually associated with an increase in free energy. This is due to that the configurational entropy, which acts as driving force for point defect formation, is significantly smaller for grain boundaries and other defects of higher order [108]. Grain boundaries form as a consequence of the lattice mismatch between grains that occur during crystal growth.

The increase in energy per area unit upon formation of a stoichiometric grain boundary is given by

$$\gamma_\mathrm{GB} = \frac{G_\mathrm{GB} - G_0}{A}, \tag{3.41}$$

where G_GB is the free energy of the system hosting the grain boundary and A is the grain boundary area. For a non-stoichiometric boundary the expression for the interface energy becomes more complicated as it then also depends on the chemical potential of the constituent atoms.

A consequence of the structure being different at grain boundaries is that defect formation energies often differ there as well. It is therefore practical to introduce a spatial dependence in the formation energy and Eq. (3.33) can then be written as

$$\Delta G^\mathrm{f}_\mathrm{def}(\boldsymbol{R}_i) = G_\mathrm{def}(\boldsymbol{R}_i) - G_0(\boldsymbol{R}_i) - \sum_i \Delta n_i \mu_i + q\mu_\mathrm{e}, \tag{3.42}$$

where $G_0(\boldsymbol{R}_\mathrm{Bulk}) = G_0$ and $G_0(\boldsymbol{R}_\mathrm{GB}) = G_\mathrm{GB}$. With this equation it is possible to express the segregation energy, which is the difference in the formation energy at the bulk and grain boundary, as

$$\Delta G^\mathrm{seg}_\mathrm{def} = \Delta G^\mathrm{f}_\mathrm{def}\left(\boldsymbol{R}_\mathrm{GB}\right) - \Delta G^\mathrm{f}_\mathrm{def}\left(\boldsymbol{R}_\mathrm{Bulk}\right). \tag{3.43}$$

$\Delta G^\mathrm{seg}_\mathrm{def} < 0$ indicates that it is more favorable to form defects at the grain boundary while positive energies suggest the opposite. Negative segregation energies are the driving force for space-charge formation, which is the topic of the next section.

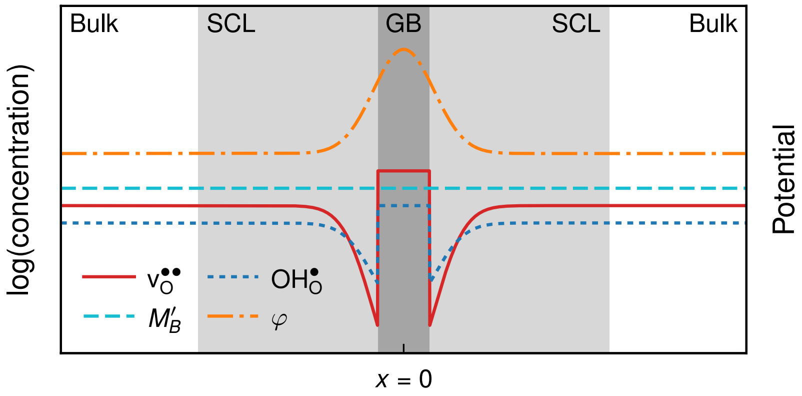

Figure 3.3: A schematic representation of space-charge formation, where the grain boundary (GB) and the bulk region are separated by a space-charge layer (SCL). The considered defect species are typical for proton conducting perovskite oxides: doubly charged oxygen vacancies ($v_O^{\bullet\bullet}$), protons ($OH_O^{\bullet}$), and B-site acceptor dopants (M_B').

3.6 Space-charge modeling

The accumulation of charged defects in a material can give rise to charged regions in space and is referred to as space-charge formation. This phenomenon occurs in acceptor-doped $BaZrO_3$ (and many other oxides as well) where it leads to high grain boundary resistance (see Section 2.2). A schematic representation of space charge formation at a grain boundary is shown in Fig. 3.3, where point defects typical for proton conducting perovskites are considered. Charged defects (oxygen vacancies and protons in this case) segregate to the grain boundary due to a negative segregation energy, which increase the defect concentration at the grain boundary core (note the log scale in Fig. 3.3). This leads to a net charge at the core that gives rise to an electrostatic potential. The potential depletes the surrounding regions (the space-charge layers) of defects with the same charge polarity, which are oxygen vacancies, protons, and possibly holes in the present example. In turn, this reduces the conductivity across the boundary since it is proportional to the defect concentrations.

Describing space-charge formation requires a thermodynamic model that include electrostatic defect interactions. It is possible to derive such a model based on the *electrochemical potential*. In Sections 3.1 and 3.2 the chemical potential for a defect was derived on the basis of the configurational entropy. The same approach can be used to obtain the electrochemical potential for a defect of species i with charge q_i in an electrostatic potential φ, which is given by

$$\mu_i(x) = \mu_i^\circ(x) + q_i\varphi(x) + kT \ln \frac{c_i(x)}{c_i^{\max}(x) - c_i(x)}, \tag{3.44}$$

where a one-dimensional spatial dependence (x) has been introduced. For neutral defects this expression becomes equivalent to the expression for the chemical potential in Eq. (3.13).

Assume that a grain boundary (or any other interface) is located at $x = 0$. The grain interior is then located at $x \approx \infty$, far from the boundary. In equilibrium the chemical potential should be constant throughout the material, which can be stated as $\mu_i(x) = \mu_i(\infty)$. This condition together with Eq. (3.44) leads to

$$\frac{c_i(x)}{c_i^{\max}(x) - c_i(x)} = \frac{c_i(\infty)}{c_i^{\max}(\infty) - c_i(\infty)} \exp\left(-\frac{\Delta\mu_i^\circ(x) + q_i\Delta\varphi(x)}{kT}\right), \tag{3.45}$$

where $\Delta\mu_i^\circ(x) = \mu_i^\circ(x) - \mu_i^\circ(\infty)$ corresponds to the segregation energy and $\Delta\varphi(x) = \varphi(x) - \varphi(\infty)$ is the space-charge potential. The latter can be obtained by solving Poisson's equation

$$\frac{\mathrm{d}^2}{\mathrm{d}^2 x}\Delta\varphi(x) = -\frac{1}{\varepsilon}\rho(x), \tag{3.46}$$

where ε is the dielectric function and $\rho(x)$ is the charge density, which is given by

$$\rho(x) = \sum_i q_i c_i(x). \tag{3.47}$$

The set of coupled equations that are Equations 3.45-3.47 can be solved in an iterative, self-consistent manner in order to obtain equilibrium defect concentrations and the corresponding space-charge potential.

The space-charge model described above has been employed to acceptor-doped $BaZrO_3$ and $BaCeO_3$ in Papers I-IV. While all four papers consider a scenario where the dopant concentration is assumed to be constant throughout the material, which is referred to as the *Mott-Schottky approximation* (see Fig. 3.3), only Paper III treats the case where dopants are mobile and can respond to the potential. In previous theoretical studies on space-charge formation the grain boundary core have been treated as a uniform region associated with one single segregation energy for each considered defect [72, 73, 77, 109]. In Paper I a more elaborate model is formulated where the core is divided into layers and where each layer contains one or several sites for each defect species. In turn, each site is associated with a segregation energy that have been determined from first-principles calculations using Eq. (3.43). This model was also used in Papers II and IV but not in Paper III, since only one segregation site was considered in that study.

4

Conductivity

In general, the conductivity of a charge carrier can be expressed as

$$\sigma = \frac{A}{T} \exp\left(-\frac{E^{\mathrm{a}}}{kT}\right), \tag{4.1}$$

where A is a prefactor and E^{a} is the activation energy. Many factors influence these two quantities and these will to some extent be elucidated in this chapter.

There are two main properties of a charge carrier besides the charge that determines its conductivity: the *concentration* and the *mobility*. Under the assumption of non-interacting charge carriers the conductivity of a carrier i can be written as

$$\sigma_i = q_i B_i n_i, \tag{4.2}$$

where n_i is the charge carrier concentration, B_i is the mobility and q_i is the charge. The previous chapter focused on defect concentrations, both in bulk structures and at interfaces. This chapter will put emphasis towards the other contributor to the conductivity, the carrier mobility.

The mobility depends on a variety of properties. Charge carriers can have different conduction mechanisms depending on the nature of the carrier as well as the crystal structure of the material. For instance, the conduction mechanisms of protons and oxide ions in perovskites are different. Higher order defects (e.g., surfaces, interfaces and grain boundaries) can be associated with mobilities that are different compared to the bulk, which can lead certain conduction pathways and networks through the material. There is also the possibility that defects in the material interact with the carrier and influence the mobility. This is rather likely when defect concentrations are high such as in acceptor-doped perovskites. For instance, yttrium ions have been found to act as trap sites for protons in yttrium-doped $\mathrm{BaZrO_3}$, which have a reducing effect on the proton conductivity [110].

The following two sections will consider the conduction mechanisms of some defects that have studied in this thesis. The first one discusses ionic conduction with focus on oxide ions (oxygen vacancies) and protons, while the second section covers conduction of electrons and holes. The following text is just a short summary of the topic and more a more detailed theoretical description can be found in textbooks on the subject, such as [108, 111, 112].

4.1 Ionic conduction

The mobility of an ion is related to the self-diffusion coefficient D through the Nernst-Einstein relation [113]

$$B = \frac{qD}{kT}. \tag{4.3}$$

By making the assumption that ionic diffusion in a material resembles that of a three-dimensional random walk the diffusion coefficient can be expressed as

$$D = \alpha Z N_\mathrm{s} \nu \exp\left(-\frac{\Delta G^\mathrm{m}}{kT}\right) = \alpha Z N_\mathrm{s} \nu \exp\left(\frac{\Delta S^\mathrm{m}}{k}\right) \exp\left(-\frac{\Delta H^\mathrm{m}}{kT}\right) \tag{4.4}$$

where Z is the number of adjacent sites available for migration, N_s is the fraction of those sites that are empty, ν is an attempt frequency that represents how often the ion will try to migrate, and $\Delta G^\mathrm{m} = \Delta H^\mathrm{m} - T\Delta S^\mathrm{m}$ is the free energy of migration. Finally, α is a parameter that includes geometric factors, such as crystal structures and lattice constants, as well as a correlation factor that accounts for non-randomness in the diffusion. In perovskites both oxide ions and protons diffuse on the oxygen sub lattice, although though different mechanisms, and thereby does Z correspond to the number of neighboring oxygen sites.

The character of the diffusion mechanism is reflected in N_s. For oxide ions it is only possible to move to a nearby vacant site. N_s therefore corresponds to the fractional concentration of oxygen vacancies in the material and can be written as $N_\mathrm{s} = c_\mathrm{v}/N_\mathrm{O}$, where c_v and N_O are the concentration of vacancies and oxygen lattice sites. As an oxide ion moves into a vacant site the initial site becomes empty (see Fig. 4.1). Instead of having an oxide ion moving in one direction, it can be thought of as if the oxygen vacancy is the diffusing species, moving in the opposite direction. This view is more common as the concentration of vacancies is much smaller than the concentration of oxide ions. It then follows that $N_\mathrm{s} = c_\mathrm{O}/N_\mathrm{O}$, where c_O is the oxide ion concentration. Typical migration enthalpies (ΔH^m) for oxide ions in perovskites are found within the range 0.6-1.0 eV [46, 114].

Like oxygen vacancies, protons in perovskite oxides also migrate between neighboring oxygen sites, although through completely different mechanism. When introduced into the material [see Eq. (2.3)] the proton forms a O-H bond with a

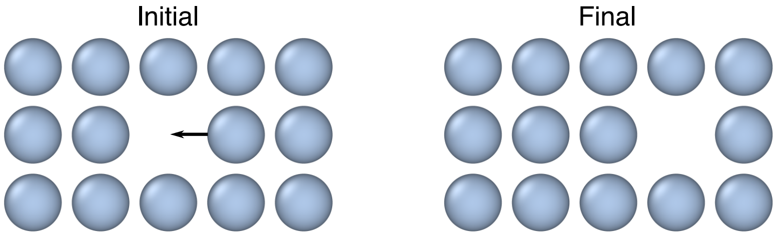

Figure 4.1: A schematic representation of the vacancy diffusion mechanism. The missing ion corresponds to the vacancy. When the ion moves to the left the vacancy moves in the opposite direction to the right.

nearby oxygen and create a hydroxide ion. The proton can then move around between different sites through a step-wise structural diffusion process, which is often referred to as a Grotthuss-like mechanism [45, 115]. More explicitly, the proton can both rotate around the oxide ion and transfer between two adjacent oxide ions (e.g, as depicted in Fig. 4.2), which for $BaZrO_3$ are associated with similar migration enthalpies [116, 117]. As the proton moves from one oxide ion to another the number of available sites for diffusion is also given by $N_s = c_O/N_O$. Proton migration enthalpies in perovskites are usually lower than the oxide ion counterpart and typically range between 0.4-0.6 eV [45, 46]. These lower migration barriers are the reason for why solid oxide proton conductors can operate at intermediate temperatures.

By combing Equations (4.2), (4.3) and (4.4) it is possible to derive an explicit expression for the conductivity. Assuming a small defect concentration ($N_s \approx 1$) we obtain

$$\sigma_i = \frac{q_i^2 c_i \alpha Z \nu_i \exp\left(\Delta S_i^{\mathrm{m}}/k\right)}{kT} \exp\left(-\frac{\Delta H_i^{\mathrm{m}}}{kT}\right). \tag{4.5}$$

Comparing this expression with Eq. (4.1) would at first glance suggest that there is a one-to-one correspondence between the activation energy and the migration barrier. This is true if the defect concentration is fixed. This is not always the case, which was shown in the previous chapter, and in many cases does the concentration c_i follow an exponential temperature dependence. In the dilute limit the concentration is given by Eq. (3.11) and Eq. (4.5) can then be written as

$$\sigma_i = \frac{q_i^2 c_i^{\max} \alpha Z \nu_i \exp\left[\left(\Delta S_i^{\mathrm{m}} + \Delta S_i^{\mathrm{f}}\right)/k\right]}{kT} \exp\left(-\frac{\Delta H_i^{\mathrm{m}} + \Delta H_i^{\mathrm{f}}}{kT}\right). \tag{4.6}$$

Comparing this expression with Eq. (4.1) indicate that

$$E_{\mathrm{a},i} = \Delta H_i^{\mathrm{m}} + \Delta H_i^{\mathrm{f}}, \tag{4.7}$$

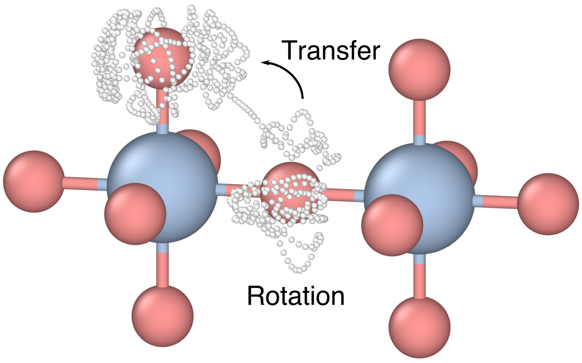

Figure 4.2: Proton trajectory that shows the two steps of the proton diffusion mechanism in perovskite oxides: rotation and transfer. Red, white and blue atoms represent oxygen, hydrogen and the B-site species, respectively.

which means that the activation energy depends both on the migration barrier and the defect formation energy. More complicated expressions for the concentration [e.g., Eq. (3.20) and Eq. (3.24)] depends on the equilibrium constant and consequently does the free energy of the corresponding reaction enter into the activation energy. Additionally, these expressions follow a non-exponential dependence on external parameters such the partial pressures and dopant concentrations, which then contribute to the prefactor.

4.2 Electronic conduction

Similar to the activated diffusion of ions [Eq. (4.3) and Eq. (4.4)] the mobility of electron and holes can in general be written as

$$B = B_0(T)\exp\left(-\frac{\Delta H^{\mathrm{m}}}{kT}\right), \tag{4.8}$$

where the prefactor $B_0(T)$ contains all contributions to the mobility except for the migration barrier. The form of $B_0(T)$ and the typical height of ΔH^{m} depend on the character of the electronic carrier. For delocalized electrons and holes with a band conduction mechanism there is no migration barrier to overcome and the mobility can generally written as $B = B_0(T)$, whose form depend on active scattering mechanisms [108]. In semiconductors and insulators, scattering is mainly due to ionized impurities at low temperatures for which $B_0(T) \propto T^{3/2}$. At high temperatures lattice vibrations play a dominant role, which lead to $B_0(T) \propto T^{-3/2}$.

The picture is slightly different for localized carriers as these are associated with finite migration barriers. While the mobility for large polarons is similar to that of band conduction as their migration barriers are quite low, small polarons behave more like ions and migration barriers are typically larger. An important distinction from ionic migration, however, is that the localized charge can transfer both *adiabatically* and *diabatically* [111]. Adiabatic transfer refers to when the local distortion follows the charge and can be treated in the same way as ionic migration using the methodology of the previous section. A diabatic transfer event, on the other hand, is much faster and there is not enough time for ions to respond to the charge before the carrier moves on to another site. For diabatic migration the mobility is given by

$$B(T) = \frac{q}{kT}\alpha v \pi^{3/2} \eta \exp\left(-\frac{\Delta H^{\mathrm{m}} + J}{kT}\right), \tag{4.9}$$

where α and v have a similar meaning as in Eq. (4.4), ΔH^{m} is the adiabatic migration barrier, and J is the electronic coupling between the initial and final states. η is given by

$$\eta = \frac{J^2}{v\sqrt{(\Delta H^{\mathrm{m}} + J)kT}} \tag{4.10}$$

and is a measure of the adiabaticity, where $\eta > 1$ validates an adiabatic approach.

In the same way as for the ionic conductivity, the carrier concentration may also follow an exponential temperature dependence that contribute to the activation energy, such as Eq. (3.29) and Eq. (3.30). For the explicit case of band state holes in acceptor-doped perovskites, the concentration is given by Eq. (3.22) that together with a band-like mobility leads to

$$E_{\mathrm{a}} = \frac{\Delta H^{\circ}_{\mathrm{ox}}}{2}, \tag{4.11}$$

where $\Delta H_{\mathrm{ox}}{}^{\circ}$ is the oxidation enthalpy. If the hole instead forms a polaron that moves adiabatically, then the activation energy is given by

$$E_{\mathrm{a}} = \frac{\Delta H^{\circ}_{\mathrm{ox}} + 2\Delta H^{\mathrm{f}}_{\mathrm{pol}}}{2} + \Delta H^{\mathrm{m}}. \tag{4.12}$$

5

Computational methods

A theoretical description of matter is essential in order to understand the structural and chemical properties of materials. On the atomic scale, any property of a system of interacting particles should be possible to obtain from the corresponding quantum mechanical wave function $\Psi(\boldsymbol{r}_1, \boldsymbol{r}_2, \dots, \boldsymbol{R}_1, \boldsymbol{R}_2, \dots; t)$, where $\boldsymbol{r}_i$ and $\boldsymbol{R}_I$ denote the position of electron i and nucleus I, respectively, while t is time. The wave function can in principle be obtained by solving the time-independent Schrödinger equation

$$H\Psi_n(\boldsymbol{r}_1, \boldsymbol{r}_2, \dots, \boldsymbol{R}_1, \boldsymbol{R}_2, \dots) = E_n\Psi_n(\boldsymbol{r}_1, \boldsymbol{r}_2, \dots, \boldsymbol{R}_1, \boldsymbol{R}_2, \dots), \tag{5.1}$$

where the Hamiltonian is given by (in atomic units: $\hbar = e = m_\mathrm{e} = 4\pi\varepsilon_0 = 1$)

$$\begin{aligned} H = &-\frac{1}{2}\sum_i \nabla_i^2 + \frac{1}{2}\sum_{i\neq j}\frac{1}{|\boldsymbol{r}_i - \boldsymbol{r}_j|} - \sum_{i,I}\frac{Z_I}{|\boldsymbol{r}_i - \boldsymbol{R}_I|} \\ &-\frac{1}{2}\sum_I \frac{\nabla_I^2}{M_I} + \frac{1}{2}\sum_{I\neq J}\frac{Z_I Z_J}{|\boldsymbol{R}_I - \boldsymbol{R}_J|}, \end{aligned} \tag{5.2}$$

where M_I and Z_I denote mass and charge of the nuclei. The first and fourth terms on the right-hand side of this equation correspond to the kinetic energy of electrons and nuclei, respectively, while the other terms represent Coulombic interactions. Finding an exact solution to Eq. (5.1) is an extremely difficult task, which is only possible for single atoms and small molecules. Most problems of interest are associated with much larger system sizes and approximations are therefore needed.

A first approximation, which is the starting point for many methods, is to treat electrons and nuclei separately. This is referred to as the Born-Oppenheimer approximation [118] ,which is applicable since the nuclei are much heavier compared to the electrons and electron dynamics are thus significantly faster. In many situations it is therefore reasonable to assume that the electrons can relax into the ground state of any given atomic configuration.

The Hamiltonian of the electronic problem is given by

$$H_\mathrm{e} = -\frac{1}{2}\sum_i \nabla_i^2 + \frac{1}{2}\sum_{i \neq j} \frac{1}{\left|\boldsymbol{r}_i - \boldsymbol{r}_j\right|} + V_\mathrm{ext}, \tag{5.3}$$

where V_ext is the external potential from the nuclei. Solving the Schrödinger equation for the electrons is still a formidable problem, and more approximations are needed to obtain a solution. Sections 5.1 and 5.2 describe two different approaches to solve this equation at different levels of approximations and accuracy: *density-functional theory* and the *GW-approximation*. The nuclear problem, which is covered in Section 5.4, is often approached with the assumption that quantum mechanical effects are small and it is therefore reasonable to consider a classical treatment of the nuclei.

5.1 Density-functional theory

Density-functional theory (DFT) is a first-principles method that revolves around the electron density $n(\boldsymbol{r})$. It can be shown (see Section 5.1.1) that if the ground state density is known then everything about the ground state is known. The density is obtained by integrating the electronic wave function over all coordinates except one:

$$n(\boldsymbol{r}) = \int \cdots \int \Psi^*(\boldsymbol{r}, \boldsymbol{r}_2, \ldots, \boldsymbol{r}_N)\Psi(\boldsymbol{r}, \boldsymbol{r}_2, \ldots, \boldsymbol{r}_N)\mathrm{d}\boldsymbol{r}_2 \ldots \mathrm{d}\boldsymbol{r}_N. \tag{5.4}$$

By considering the electron density instead of the corresponding wave function the degrees of freedom in a system with N electrons are reduced from $3N$ to 3. This results in a much more tractable problem.

Modern DFT relies upon a theoretical framework that was derived by Walter Kohn and coworkers in the 1960s, for which he was awarded the Nobel Prize in Chemistry in 1998. A short summary of this theory is described in the following sections, with emphasis on extended systems. For a more thorough description of DFT see, e.g., [119–122].

5.1.1 Theoretical background

In 1964 Hohenberg and Kohn [123] formulated and proved two theorems that make up the foundation of modern DFT for the electronic structure problem. What they essentially state is that Eq. (5.4) can be reversed for the ground state density:

if the ground state density $n_0(\boldsymbol{r})$ is known then so is the ground state wave function $\Psi_0(\boldsymbol{r}, \boldsymbol{r}_2, \ldots, \boldsymbol{r}_N)$ and consequently all ground state properties.

The first theorem states that the non-degenerate ground state wave function is a unique functional of the ground state density: $\Psi_0(\boldsymbol{r}_1, \boldsymbol{r}_2, \ldots, \boldsymbol{r}_N) = \Psi[n_0(\boldsymbol{r})]$. It follows that the ground state expectation value of any observable, including the ground state energy E_0, is a functional of $n_0(\boldsymbol{r})$ as well:

$$E_0 = E[n_0(\boldsymbol{r})] = \langle \Psi[n_0(\boldsymbol{r})] | \, H_\mathrm{e} \, | \Psi[n_0(\boldsymbol{r})] \rangle \, . \tag{5.5}$$

The second theorem states that there exists a functional for the energy of the form

$$E[n(\boldsymbol{r})] = F[n(\boldsymbol{r})] + \int n(\boldsymbol{r}) V_\mathrm{ext}(\boldsymbol{r}) \mathrm{d}\boldsymbol{r}, \tag{5.6}$$

which is minimized by the ground state density. $F[n(\boldsymbol{r})]$ contains the contributions from the kinetic energy and the electron-electron interactions. The functional is variational and the minimum corresponds to the ground state energy:

$$E[n_0(\boldsymbol{r})] \leq E[n(\boldsymbol{r})]. \tag{5.7}$$

Even if the problem has been simplified to finding the minimum of a functional with respect to a 3-dimensional function instead of solving the $3N$-dimensional system $\langle \Psi_0(\{\boldsymbol{r}_i\}) | \, H_\mathrm{e} \, | \Psi_0(\{\boldsymbol{r}_i\}) \rangle$ the solution is still difficult to obtain. This follows from that $F[n(\boldsymbol{r})]$ contains complex many-body effects, the exact representation of which is not known.

Further advances were made in 1965 when Kohn and Sham [124] derived a scheme that makes it possible to determine the ground state density and the corresponding energy. The key concept is that a system consisting of *interacting* electrons can be transformed into a system of *non-interacting* electrons, which is much easier to solve. In practice, this is done by writing $F[n(\boldsymbol{r})]$ in the form

$$F[n(\boldsymbol{r})] = T_\mathrm{s}[n(\boldsymbol{r})] + E_\mathrm{H}[n(\boldsymbol{r})] + E_\mathrm{xc}[n(\boldsymbol{r})], \tag{5.8}$$

where $T_\mathrm{s}[n(\boldsymbol{r})]$ is the kinetic energy of the non-interacting electrons, $E_\mathrm{H}[n(\boldsymbol{r})]$ is the Hartree energy

$$E_\mathrm{H}[n(\boldsymbol{r})] = \frac{1}{2} \iint \frac{n(\boldsymbol{r}) n(\boldsymbol{r}')}{|\boldsymbol{r} - \boldsymbol{r}'|} \mathrm{d}\boldsymbol{r} \mathrm{d}\boldsymbol{r}', \tag{5.9}$$

and $E_\mathrm{xc}[n(\boldsymbol{r})]$ is the exchange-correlation (XC) functional. The latter is defined by Eq. (5.8) and contains all complicated many-body effects. Based on this expression for $F[n(\boldsymbol{r})]$, the interacting electrons can be treated as non-interacting electrons moving in the effective potential

$$V_\mathrm{eff}(\boldsymbol{r}) = V_\mathrm{ext}(\boldsymbol{r}) + V_\mathrm{H}(\boldsymbol{r}) + V_\mathrm{xc}(\boldsymbol{r}), \tag{5.10}$$

where $V_{\mathrm{H}}(\boldsymbol{r})$ is the Hartree potential

$$V_{\mathrm{H}}(\boldsymbol{r}) = \int \frac{n(\boldsymbol{r}')}{|\boldsymbol{r}-\boldsymbol{r}'|}\mathrm{d}\boldsymbol{r}' \tag{5.11}$$

and where the XC potential $V_{\mathrm{xc}}(\boldsymbol{r})$ is the functional derivate of $E_{\mathrm{xc}}[n(\boldsymbol{r})]$:

$$V_{\mathrm{xc}}(\boldsymbol{r}) = \frac{\delta E_{\mathrm{xc}}[n(\boldsymbol{r})]}{\delta n(\boldsymbol{r})}. \tag{5.12}$$

This gives rise to the Kohn-Sham equations, a set of Schrödinger equations for non-interacting electrons

$$\left[-\frac{1}{2}\nabla^2 + V_{\mathrm{eff}}(\boldsymbol{r})\right]\psi_i(\boldsymbol{r}) = \epsilon_i\psi_i(\boldsymbol{r}) \tag{5.13}$$

that are coupled through the electron density

$$n(\boldsymbol{r}) = \sum_i f_i\,|\psi_i(\boldsymbol{r})|^2\,, \tag{5.14}$$

where f_i is the occupation of the electron state corresponding to $\psi_i(\boldsymbol{r})$. Since the single particle wave functions $\psi_i(\boldsymbol{r})$ depend on $V_{\mathrm{eff}}(\boldsymbol{r})$, which in turn depends on $n(\boldsymbol{r})$, these equations have to be solved in an iterative self-consistent manner. The solution corresponds to the ground state density $n_0(\boldsymbol{r})$ from which the ground state energy is determined according to

$$E_0 = \sum_i f_i\epsilon_i + E_{\mathrm{xc}}[n_0(\boldsymbol{r})] - \int V_{\mathrm{xc}}(\boldsymbol{r})n_0(\boldsymbol{r})\mathrm{d}\boldsymbol{r} - \frac{1}{2}\iint \frac{n_0(\boldsymbol{r})n_0(\boldsymbol{r}')}{|\boldsymbol{r}-\boldsymbol{r}'|}\mathrm{d}\boldsymbol{r}\mathrm{d}\boldsymbol{r}'. \tag{5.15}$$

The Kohn-Sham approach simplifies the problem considerably, and yet no approximations have been made. Finding the exact solution is, however, still a difficult problem due to the complex, unknown form of $E_{\mathrm{xc}}[n(\boldsymbol{r})]$. Approximations of $E_{\mathrm{xc}}[n(\boldsymbol{r})]$ are therefore needed in order to proceed any further. This is the topic of the next section.

5.1.2 Exchange-correlation functionals

Many approximations of the XC functional have been suggested over the years with varying level of complexity, where the sophistication of the functional generally goes hand in hand with both higher accuracy and a larger computational cost. This section will cover some of the most common approximations. While spin is generally included in these formulations it is left out here for brevity.

The simplest approximation is the *local density approximation* (LDA), which was proposed by Kohn and Sham in their original paper [124]. Within this approximation the XC energy is given by

$$E_{\mathrm{xc}}^{\mathrm{LDA}}[n(\boldsymbol{r})] = \int n(\boldsymbol{r})\epsilon_{\mathrm{xc}}^{\mathrm{LDA}}[n(\boldsymbol{r})]\mathrm{d}\boldsymbol{r}, \tag{5.16}$$

where $\epsilon_{\mathrm{xc}}^{\mathrm{LDA}}[n(\boldsymbol{r})]$ is the XC energy density of a uniform electron gas with density $n(\boldsymbol{r})$. In spite of its simplicity, this approximation works remarkably well for a wide range of systems and properties when parametrized with data from quantum Monte Carlo simulations [125].

The electron density of most materials is inhomogeneous and a natural next step beyond LDA is to take variations in the density into account. The practical approach is the semi-local *generalized gradient approximation* (GGA), where the XC energy also takes the gradient of the density into account:

$$E_{\mathrm{xc}}^{\mathrm{GGA}}[n(\boldsymbol{r})] = \int n(\boldsymbol{r})\epsilon_{\mathrm{xc}}^{\mathrm{GGA}}[n(\boldsymbol{r}), \nabla n(\boldsymbol{r})]\mathrm{d}\boldsymbol{r}. \tag{5.17}$$

The gradient can be incorporated in many different ways and there exists a wide range of different GGAs. There are two main approaches to functional development: derivations based on theoretical arguments where the functional is forced to obey constraints set by known features of the exact functional, and semi-empirical schemes where one or several parameters are fitted to reproduce experimental results of desired properties, usually energy differences. The former methodology generally leads to functionals with higher transferability that reproduce electron densities more accurately [126]. The GGA functional PBE [127] belongs to this category and is one of the most popular functionals for materials. This functional has been used in all but the last paper in this thesis. Empirically fitted functionals are more frequently used in quantum chemistry. The GGAs improve on LDA in many aspects, such as cohesive energies and bond lengths. There are, however, some systems and properties that are better described with LDA.

Although the local and semi-local functionals manage to predict many properties with reasonable accuracy, they systematically fail in some cases. Van der Waals interactions, which results from non-local correlations, belong to this category. The desire for finding an efficient description of these interactions has increased in recent years due to the emergence of layered 2D materials and many attempts have been made to develop functionals that include these effects. One such functional class is the van der Waals density functional (vdW-DF) method [128], which is constraint-based and builds upon GGAs. The latest installment of this functional, abbreviated vdW-DF-cx with cx for consistent exchange [129], works well for both dense and sparse systems [130, 131] and has been used in Paper IX.

Two other systematic failures of LDA and GGAs that are central this thesis are the inability to predict accurate band gaps and localized states in semiconductors and insulators. These two problems have similar origins and can therefore be treated with similar methods, which will be discussed in the following section.

5.1.3 Limitations of LDA and GGA

LDA and GGAs suffer from two severe problems that impair the description of semiconductors and insulators: the systematic underestimation of band gaps by up to about 40-50%, which is referred to as the *band gap problem*, and the inability to properly describe localized states. Both these errors are manifestations of that these functionals incorrectly describe systems with fractional charges [132, 133], or in other words, derivates of the functionals with respect to charge are not well described.

It has been shown [134] that the exact Kohn-Sham functional is *piecewise linear*: the total energy $E(N)$ consists of straight line segments with discontinuities at integer values of N (see Fig. 5.1). Approximate functionals, on the other hand, generally deviate from piecewise linearity by displaying either a convex or concave curvature for fractional charges, which leads to erroneous delocalization or overlocalization, respectively. LDA and GGAs belong to the former, thus suffering from a delocalization error. This error originates from a spurious self-interaction that is introduced by the Hartree term, see Eq. (5.9). While the exact XC functional cancels this error this is not the case for LDA and GGAs.

The fundamental band gap of an insulator or semiconductor is given by

$$E_{\text{gap}} = I - A = [E(N-1) - E(N)] - [E(N) - E(N+1)], \tag{5.18}$$

where I is the ionization energy and A is the electron affinity. The gap can also be expressed in terms of derivatives of the Kohn-Sham functional

$$E_{\text{gap}} = \lim_{\delta N \to 0} \left(\frac{\delta E}{\delta n}\bigg|_{N+\delta N} - \frac{\delta E}{\delta n}\bigg|_{N-\delta N} \right). \tag{5.19}$$

This expression indicates that the band gap originates from a derivate discontinuity in the total functional. Since LDA and GGAs deviate from the piecewise linear behavior with a convex curvature, it follows that the first derivate at $N+\delta N$ decreases while the second one at $N-\delta N$ increases, which leads to an underestimation of the band gap (see Fig. 5.1).

Furthermore, for the exact functional Eq. (5.19) yields

$$E_{\text{gap}} = \epsilon_{\text{gap}}^{\text{KS}} + \Delta_{\text{xc}}, \tag{5.20}$$

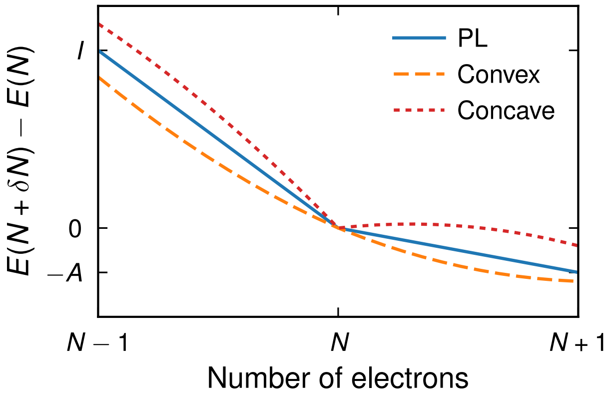

Figure 5.1: Schematic representation of the piecewise linear (PL) behavior of the exact functional. A convex curvature, which is typical for LDA and GGAs, leads to a delocalization error and an underestimation of the band gap. A concave behavior, which is the case for Hartree-Fock, results in over-localization and overestimated band gaps.

where $\epsilon_{\text{gap}}^{\text{KS}}$ is the band gap of the Kohn-Sham energy spectrum and Δ_{xc} is the derivative discontinuity in the xc-functional:

$$\Delta_{\text{xc}} = \left.\frac{\delta E_{\text{xc}}}{\delta n}\right|_{N+\delta N} - \left.\frac{\delta E_{\text{xc}}}{\delta n}\right|_{N-\delta N} = V_{\text{xc}}|_{N+\delta N} - V_{\text{xc}}|_{N-\delta N} \,. \tag{5.21}$$

While $\epsilon_{\text{gap}}^{\text{KS}}$ stems from the kinetic energy of the non-interacting particles [T_{s} in Eq. (5.8)], which is exact, Δ_{xc} depends on the approximation of E_{xc} and varies accordingly. V_{xc} is continuous for LDA and GGA functionals (or any other functional without an explicit orbital dependence [133]) and consequently is $\Delta_{\text{xc}} = 0$. This also leads to an underestimation of the band gap since $\Delta_{\text{xc}} > 0$ for the exact functional [135–137].

Besides affecting the band gap, the self-interaction error has a severe impact on highly localized electron orbitals, especially those representing *d*- and *f*-electrons but *p*-electrons are also affected. This is particularly problematic for transition metal oxides where both the valence and conduction bands derive from these states. As a consequence, LDA and GGA fail to describe polaronic states of electrons and holes in these materials.

Different approaches that go beyond LDA and GGAs have been proposed to remedy the band gap problem and the delocalization error, and since both errors appear related some of these methods treat both problems simultaneously. The remainder of this section outlines such methods that have been considered in this thesis, with the exception of the G_0W_0 method, which is the only non-DFT approach and is covered in Section 5.2.

5.1.3.1 DFT+*U*

One of the most widely used approaches to treat self-interaction is the DFT+U method [138, 139] (originally LDA+U), where an on-site correction U is applied to specific orbitals that penalizes partial occupation:

$$E_{\mathrm{DFT}+U} = E_{\mathrm{DFT}} + \frac{1}{2}\sum_{\alpha,I} U_\alpha n_{\alpha,I}(1 - n_{\alpha,I}), \tag{5.22}$$

where $n_{I,\alpha}$ is the occupancy of the orbital α at the atomic site I. It is evident from the quadratic form of the correction term that the U parameters can be chosen such that the convex curvature of $E(N)$ diminishes and piecewise linearity is obtained. While DFT+U treats the self-interaction in a rather simple and efficient manner a major concern with the method lies within the choice of the U parameters. The appropriate value of U is strongly dependent of the atomic configuration and can even vary for different local environments within the same material, such as for the same defect in supercells with different sizes. In addition, the value of U depends on the choice of the XC functional and the overall transferability of the method is therefore quite limited. In practice, it is quite common that U is determined by empirical fitting to reproduce experimental data such as band gaps or XPS data. It is, however, possible to determine U purely on theoretical grounds by, e.g., constraining localized orbital occupations [140, 141]. When modeling polarons, it is also quite common to determine U self-consistently for the polaronic configuration by enforcing on the polaronic level either a Koopmans-like condition [142] or piecewise linearity explicitly [143]. Beside the ambiguity of the choice of U, another problem with DFT+U lies in the fact that it is an *on-site* correction and it therefore cannot fully capture localization between atoms, such as bond-centered polarons (e.g., V_K centers in alkali halides).

5.1.3.2 Hybrid functionals

Another common approach to treat the band gap problem and self interaction is to use *hybrid functionals*. Hybrid functionals [144–146] are a class of functionals that substitute a part of the DFT exchange with Hartree-Fock (HF) [147] exchange, giving an XC functional of the form

$$E_{\mathrm{xc}}^{\mathrm{hybrid}} = E_{\mathrm{xc}}^{\mathrm{DFT}} + \alpha\left(E_{\mathrm{x}}^{\mathrm{HF}} - E_{\mathrm{x}}^{\mathrm{DFT}}\right), \tag{5.23}$$

where α is the mixing parameter. The motivation for this approach is that HF, in contrast to LDA and GGAs, displays a concave curvature at fractional charges (see Fig. 5.1) and therefore suffers from a localization error, which results in a systematic overestimation of the band gap [132]. Thus by combining LDA/GGA with HF their corresponding errors are expected to cancel, leading to a more accurate description of the band gap and charge localization. The value of α has been determined in many different ways using both theoretical and semi-empirical schemes. The most popular hybrid functionals for materials, PBE0 [148] and HSE [149, 150], both use the theoretically derived value of $\alpha = 0.25$. The HSE functional also contains a screening parameter ω that determines the range of the HF exchange in order to reduce the computational effort. In recent years, however, there have been many studies based on the PBE0 and HSE functionals where α and ω have been treated as free parameters, and they are often fitted to reproduce certain properties, such as experimental band gaps.

5.1.3.3 pSIC-DFT

A more recently developed method for treating the self-interaction error in the context of modeling small polarons is the pSIC-DFT method [151], where pSIC stands for polaron self-interaction correction. This method was used in Paper VII. The development of this method was motivated by the fact that DFT+U is unable to describe bond-centered polarons while hybrid functionals are generally too demanding for structural relaxation. The pSIC method relies on the fact that the self-interaction error of LDA and GGAs does not affect closed-shell systems considerably, and within these charge states are variations in the band structure properly described. This exploits the fact that the (missing) derivative discontinuity remains approximately constant for different ionic configurations, $\Delta_{\mathrm{xc}}[\boldsymbol{R}] \approx \Delta_{\mathrm{xc}}$ [152]. The corrected pSIC total energy for the open-shell system (with $N \pm 1$ electrons) is given by

$$E_{\mathrm{pSIC}}[N \pm 1; \boldsymbol{R}] = E_{\mathrm{DFT}}[N; \boldsymbol{R}] \pm \mu^{\pm}_{\mathrm{DFT}}[N; \boldsymbol{R}] \pm \Delta^{\pm}_{\mathrm{xc}}[N], \tag{5.24}$$

where $\mu^{\pm}_{\mathrm{DFT}}[N; \boldsymbol{R}] \pm \Delta^{\pm}_{\mathrm{xc}}[N]$ refers to the highest occupied ($-$) or lowest occupied ($+$) unoccupied level in the KS energy spectrum together with the corresponding part of the derivative discontinuity. It follows that energy differences are given by

$$\Delta E_{\mathrm{pSIC}}[N \pm 1; \boldsymbol{R}; \boldsymbol{R}'] = \Delta E_{\mathrm{DFT}}[N; \boldsymbol{R}; \boldsymbol{R}'] \pm \Delta\mu^{\pm}_{\mathrm{DFT}}[N; \boldsymbol{R}; \boldsymbol{R}'], \tag{5.25}$$

which depend solely on quantities that are well described already at the local and semi-local level of approximation.

5.1.4 Plane waves and pseudopotentials

Finding a solution to the Kohn-Sham equations in a practical calculation requires further considerations. First, a mathematical representation for the single particle wave functions is needed. There are many possible choices and the suitable one depends on the system under consideration. For extended systems it is convenient to expand the wave function in a plane wave basis and to employ periodic boundary conditions due to the repetitive nature of the crystal structure. Systems without a repeating symmetry, such as defects, can still be treated using the supercell approach. The use of periodic boundary conditions results in an infinite system but by utilizing Bloch's theorem [153] the complete basis for the wave function can be obtained by considering only the wave vectors $\boldsymbol{k}$ within the first Brillouin zone. The basis functions can then be written as a Fourier series

$$\psi_{n,\boldsymbol{k}}(\boldsymbol{r}) = \sum_{\boldsymbol{G}} c_{n,\boldsymbol{k}+\boldsymbol{G}} \exp\left[\mathrm{i}\left(\boldsymbol{k}+\boldsymbol{G}\right)\cdot\boldsymbol{r}\right], \tag{5.26}$$

where the sum is over all reciprocal lattice vectors $\boldsymbol{G}$ and n denotes the band index. Since there is an infinite set of $\boldsymbol{G}$ vectors this sum has to be truncated in order to be evaluated numerically. This is done by introducing a cut off energy E_{cut} which limits the number of $\boldsymbol{G}$ vectors according to $\frac{1}{2}\left|\boldsymbol{k}+\boldsymbol{G}\right|^2 < E_{\mathrm{cut}}$.

While the use of plane waves simplifies the problem substantially a drawback with this method is the slow convergence for rapidly oscillating wave functions near the nuclei. However, core electrons do not take part in chemical bonding and can therefore be treated differently compared to valence electrons. Additionally, a good description of the valence electrons near the nuclei is not crucial for obtaining a proper solution. For these reasons it is common to replace the potential arising from the nuclei and the core electrons with an effective potential, which is referred to as a *pseudopotential*. The pseudopotential is constructed in such a way that it produces a more smooth function within the core region, which requires a lower cut off energy, while it reproduces the all-electron wave function outside the core region. Pseudopotentials make the calculations less computationally demanding since only the valence electrons are treated explicitly. There is no restricted form for pseudopotentials as long as certain conditions are required. This has allowed for different implementations such as norm-conserving pseudopotentials [154] and ultrasoft pseudopotentials [155]. Another approach to treat the core electrons is the projector augmented wave (PAW) method [156], which has been used for all DFT calculations in this thesis. With this formalism the all-electron wave function is preserved within the core region.

5.2 *GW*-approximation

Although DFT works very well for many systems some properties, such as the band gap, are not well described (see Section 5.1.3). This calls for methods beyond the standard semi-local approximation that can describe these properties more accurately. A concept that many such methods revolve around is that of *quasiparticles*. The repulsive character of the electron-electron interaction in solids forms effectively positively charged regions around the electrons, which screen electron-electron interactions. Within this context the quasiparticle is defined as the combined entity of the electron and the positive surrounding charge. Quasiparticles interact through the screened Coulomb interaction W, which is weaker than the bare Coulomb interaction v between electrons and depends on the dielectric response of the material.

The mathematical description of quasiparticles is based on the single particle Green's function G. G is referred to as a propagator, which describes the movement of the quasiparticle. G is related to the quasiparticle wave functions Φ_i and quasiparticle energies E_i through the expression

$$G(\boldsymbol{r}, \boldsymbol{r}'; E) = \sum_i \frac{\Phi_i(\boldsymbol{r})\Phi_i^*(\boldsymbol{r}')}{E - E_i}. \tag{5.27}$$

G only depends on six spatial degrees of freedom, which makes it a more manageable quantity than the many-body wave function. The behavior of quasiparticles is governed by the quasiparticle equation

$$\left[-\frac{1}{2}\nabla^2 + V_{\mathrm{H}}(\boldsymbol{r}) + V_{\mathrm{ext}}(\boldsymbol{r})\right]\Phi_i(\boldsymbol{r}) + \int \Sigma(\boldsymbol{r}, \boldsymbol{r}'; E_i)\Phi_i(\boldsymbol{r}')\mathrm{d}\boldsymbol{r}' = E_i\Phi_i(\boldsymbol{r}), \tag{5.28}$$

where $V_{\mathrm{H}}(\boldsymbol{r})$ is the Hartree potential [see Eq. (5.11)], $V_{\mathrm{ext}}(\boldsymbol{r})$ is the external potential, and $\Sigma(\boldsymbol{r}, \boldsymbol{r}'; E)$ is the self-energy, which contains all many-body effects beyond the Hartree approximation. To obtain an analytic expression for the self-energy is not possible due to the complex nature of the many-body effects and approximations for this quantity are therefore needed. In 1965, Hedin proposed the *Hedin equations* [157], from which the self-energy in principle can be obtained in an iterative self-consistent manner. In practice, however, further approximations need to be made and the most simple one is

$$\Sigma \approx GW, \tag{5.29}$$

which has become known as the GW-approximation. The following text gives a brief outline of this method; for more comprehensive reviews on the subject see [158, 159].

Beside the expression in Eq. (5.29), G and Σ are also related through the Dyson equation

$$G = G_0 + G_0\Sigma G, \tag{5.30}$$

where G_0 is the non-interacting single particle Green's function. Similar to the expression for G in Eq. (5.27) G_0 is given by

$$G_0(\boldsymbol{r}, \boldsymbol{r}'; E) = \sum_i \frac{\psi_i(\boldsymbol{r})\psi_i^*(\boldsymbol{r}')}{E - \epsilon_i}, \tag{5.31}$$

where ψ_i and ϵ_i are the wave functions and energies for non-interacting particles, which can be obtained from, e.g., DFT or HF. Additionally, the quasiparticle energies can be expressed in terms of ϵ_i according to

$$E_i = \epsilon_i + \langle\psi_i| \Sigma(E_i) - V_{\mathrm{xc}} |\psi_i\rangle \approx \epsilon_i + Z_i \langle\psi_i| \Sigma(\epsilon_i) - V_{\mathrm{xc}} |\psi_i\rangle \,, \tag{5.32}$$

where V_{xc} is the XC potential [Eq. (5.12) for DFT] and $Z_i = [1 - \partial\Sigma_i(E)/\partial E|_{E=\epsilon_i}]^{-1}$ is the quasiparticle weight, with $\Sigma_i(E) \equiv \langle\psi_i| \Sigma(E) |\psi_i\rangle$.

The determination of Σ requires knowledge of G and vice versa, and a solution can therefore only be obtained in an iterative, self-consistent manner. An evaluation of a GW self-consistency cycle starts with a Green's function G. Based on this function the polarization P can be determined from which the dielectric function ε is obtained. In turn, the screened Coulomb interaction can be determined as $W = \varepsilon^{-1}v$ and Eq. (5.29) can then be used to determine the self-energy. Finally, a new Green's function G is obtained from Eq. (5.30). In order to perform an actual GW calculation an initial guess for G is required. In practice G_0 is used as a starting point and the resulting screened Coulomb interaction is referred to as W_0.

There are several different ways to perform GW calculations that differ in the way G and W are updated in the self-consistency cycle, which has led to a series of different notations and abbreviations. G_0W_0 refers to the perturbative approach when neither G or W are updated which corresponds to simply determining the self-energy once and then calculating E_i using Eq. (5.32). This approach has been considered in Paper I. Following the same logic, GW_0 refers to when G is updated while W is kept fixed, and GW in this context is when both G and W are updated. When updating G there is also a choice of keeping the non-interacting wave functions or updating them as well along with quasiparticle energies [160, 161]. The latter is referred to as quasiparticle self-consistent GW and is either abbreviated as QSGW or QPscGW.

An important aspect of G_0W_0 is the fact that it is a perturbative approach, which relies on the character of the initial wave functions. It thus follows that band gaps, band widths and orbital positions obtained from G_0W_0 calculations differ depending on the underlying method used to compute the initial ψ_i [162–165]. As a consequence, for certain systems when LDA or GGA are used the limitations of these methods can to some extent carry over to G_0W_0 leading to qualitative errors, such as metallic instead of semiconducting behavior or disproportional band edge shifts [162, 165].

In a practical calculation an important parameter is the number of empty bands that are included in the evaluation of the frequency dependent dielectric function [166]. While the band gap typically converges rather quickly with the number of bands individual quasiparticle energies converge much more slowly (see Paper VI). It is therefore especially important to converge the quasiparticle energy spectrum if the GW calculation is intended for correcting defect formation energies.

5.3 Defect formation energies

In Chapter 3 the thermodynamics of point defects were described, which very much revolve around the defect formation energy $\Delta G^{\mathrm{f}}_{\mathrm{def}}$. There, however, it was not specified explicitly how this quantity is obtained and this section is therefore devoted to the methodology of calculating defect formation energies and related properties within the framework of DFT. There are multiple aspects that need to be taken into account in order to avoid pitfalls that can lead to both quantitative and qualitative errors. The following text will focus on those that have been important for the work in this thesis. A more comprehensive review of point defect modeling that covers further aspects can be found in [167].

At zero temperature the formation free energy is given by

$$\Delta G^{\mathrm{f}}_{\mathrm{def}}(0) = \Delta H^{\mathrm{f}}_{\mathrm{def}}(0) = \Delta E^{\mathrm{f}}_{\mathrm{def}} + \Delta E^{\mathrm{zp}}, \tag{5.33}$$

where the PV-term has been neglected (see Section 3.4) and where $\Delta E^{\mathrm{f}}_{\mathrm{def}}$ and ΔE^{zp} are the electronic and zero-point contributions, respectively. The latter is usually quite small and requires the vibrational frequencies, which can be obtained from, e.g., phonon calculations, and has therefore often been neglected in studies where temperature effects are not considered. The former can be expressed as

$$\Delta E^{\mathrm{f}}_{\mathrm{def}} = E^{\mathrm{tot}}_{\mathrm{def}} - E^{\mathrm{tot}}_{\mathrm{ideal}} - \sum_i \Delta n_i \mu_i + q(\epsilon_{\mathrm{VBM}} + \mu_{\mathrm{e}}), \tag{5.34}$$

where $E^{\mathrm{tot}}_{\mathrm{def}}$ and $E^{\mathrm{tot}}_{\mathrm{ideal}}$ are the total energies of the defective and ideal system, respectively. In this context, the electron chemical potential μ_{e} is conventionally given with respect to the position at the valence band maximum (VBM) ϵ_{VBM}, and it is thus important to distinguish between this definition of μ_{e} and the one adopted in Chapter 3 where it refers to the absolute value of the electron chemical potential. In a similar same manner, the chemical potential of the atomic species i is given with respect to a reference state

$$\mu_i = \mu_i^{\circ} + \Delta\mu_i, \tag{5.35}$$

where μ_i° is usually chosen as the chemical potential of the elemental reference phase, which yields the upper limit $\Delta\mu_i \leq 0$. The lower bound of $\Delta\mu_i$ is set by the formation energy of the host material and various competing phases.

An important quantity that is derived from the defect formation energy is the charge transition level (CTL). The CTL corresponds to the electron chemical potential, at which the relative stability of two defect charge states is interchanged and is thus equivalent to the value at which formation energies of the two states are equal: $\Delta E^{\mathrm{f}}_{\mathrm{def}}(q_1) = \Delta E^{\mathrm{f}}_{\mathrm{def}}(q_2)$. From Eq. (5.34) it follows that the CTL is given by

$$\begin{aligned}\varepsilon(q_1/q_2) &= \frac{\Delta E^{\mathrm{f}}_{\mathrm{def}}(q_1;\mu_{\mathrm{e}}=0) - \Delta E^{\mathrm{f}}_{\mathrm{def}}(q_2;\mu_{\mathrm{e}}=0)}{q_2-q_1}\\ &= \frac{E^{\mathrm{tot}}_{\mathrm{def}}(q_1) - E^{\mathrm{tot}}_{\mathrm{def}}(q_2)}{q_2-q_1} - \epsilon_{\mathrm{VBM}}. \end{aligned} \tag{5.36}$$

It is important to remember that this *thermodynamic* transition level is not the same as the defect levels that show up in the Kohn-Sham eigenenergy spectrum.

Another quantity that follows from the formation energy is the defect segregation energy. Based on Eq. (5.34) the segregation energy in Eq. (3.43) can be expressed as

$$\Delta E^{\mathrm{seg}}_{\mathrm{def}} = \Delta E^{\mathrm{f}}_{\mathrm{def}}\left(\boldsymbol{R}_{\mathrm{GB}}\right) - \Delta E^{\mathrm{f}}_{\mathrm{def}}\left(\boldsymbol{R}_{\mathrm{Bulk}}\right) = E^{\mathrm{tot}}_{\mathrm{def}}\left(\boldsymbol{R}_{\mathrm{GB}}\right) - E^{\mathrm{tot}}_{\mathrm{def}}\left(\boldsymbol{R}_{\mathrm{Bulk}}\right), \tag{5.37}$$

where $E^{\mathrm{tot}}_{\mathrm{def}}\left(\boldsymbol{R}_{\mathrm{GB}}\right)$ and $E^{\mathrm{tot}}_{\mathrm{def}}\left(\boldsymbol{R}_{\mathrm{Bulk}}\right)$ are the total energies of a defect at the grain boundary and in the bulk, respectively. The second equality in Eq. (5.37) is valid if the same grain boundary supercell is used as the ideal configuration for both formation energies.

5.3.1 Finite size effects

The supercell approach with periodic boundary conditions has become the standard procedure for calculation of defect formation energies using Eq. (5.34). While this methodology is very well suited for perfectly repeating crystal structures, it is not always as convenient for systems with defects and can lead to significant errors if not addressed properly. More specifically, the periodic boundary conditions imply an infinite array of supercells, which, for defects, introduces interactions with the periodic images. These interactions are not present for the isolated defect and while defects occasionally do interact with other, in particular at large defect concentrations, this interplay is not taking place in such a repetitive manner. Additionally, the thermodynamic framework that was derived in Chapter 3 relies on the assumption that defects do not interact with each other and therefore, in principle, requires formation energies of individual defects.

A natural first step to eliminate these interactions is to make the size of the supercell as large as possible. This approach is usually not sufficient for defect calculations based on DFT since the method is limited to systems with a relatively small number of ions and electrons, and further treatment of these interactions is therefore often necessary. The image interactions are most prominent in charged systems due to long-range Coulomb interactions that decay slowly as L^{-1}, where L is the length of the supercell. Hence, most of the correction schemes discussed below focus on the electrostatic interactions.

A theoretical description of the finite size effects is most easily derived for point defects in a cubic lattice. There are two main types of spurious interactions: *electrostatic* and *elastic*. These typically scale as L^{-1} and L^{-3} and a simple correction is to extrapolate the formation energy to an infinite system using a fitted polynomial on the form [168, 169]

$$\Delta E^{\mathrm{f}}_{\mathrm{def}}(\infty) = \Delta E^{\mathrm{f}}_{\mathrm{def}}(L) + aL^{-1} + bL^{-3}, \tag{5.38}$$

where $\Delta E^{\mathrm{f}}_{\mathrm{def}}(\infty)$, a and b are fitting parameters. A reasonable fit requires calculation of $\Delta E^{\mathrm{f}}_{\mathrm{def}}(L)$ for several different L, which is usually not feasible for materials with larger unit cells since cubic supercells often are multiples of the former. This issue was addressed recently with a scheme that increases the number of tractable data points for fitting by constructing supercells, for which the deviation from a cubic shape (here referred to as *acubicity*) is small [170]. Another drawback is that different supercell sizes only allow for certain symmetries, which can affect the defect relaxation behavior and consequently the formation energy. An example of this are the octahedral tilts in perovskites that are suppressed in supercells with an odd repetition of unit cells (e.g., $3\times3\times3$). If such an effect leads to large variations in the formation energy then the fitting parameters will be sensitive to the choice of configurations that are included in the fit.

The limitations of the extrapolation procedure call for more elaborate correction schemes. In 1985 Leslie and Gillan [171] proposed a correction to the defect formation energy in Eq. (5.34) that corresponds to the energy of an periodic array of point charges in a neutralizing background:

$$E^{\mathrm{image}}_{\mathrm{corr}}(q) = \frac{Mq^2}{2\varepsilon L}, \tag{5.39}$$

where M is the Madelung constant and ε is the macroscopic dielectric constant. Since then more involved schemes have been suggested, with many of them including the monopole-monopole correction in Eq. (5.39) as well as additional electrostatic contributions, such as different model charge distributions and potential alignment [172–178]. The need for potential alignment, which refers to the alignment of the electrostatic potential in the defective (far from the defect) and ideal supercells, follows from a divergence in the total energy for charged systems [179]. The total energy of a neutral supercell within the periodic scheme is well defined and is determined up to an arbitrary constant. For a charged supercell, however, the total energy diverges unless the average potential is set to zero, which corresponds to adding a neutralizing background charge. This leads to a shift in the constant that in turn yields a contribution to the formation energy. This can be corrected for by adding the correction term $q\Delta V$ to Eq. (5.34), where ΔV is the difference between the potential in the defective and ideal supercells far from the defect [174]. Assessment of correction schemes has shown that they all work reasonably well for defects with localized charge distributions but not for partially or fully delocalized defects [178, 180].

Point defects have been studied in all papers in this thesis and correction schemes have therefore been an important aspect in this work. Most of the considered materials do, however, exhibit large dielectric constants and image interactions therefore become fairly small and formation energies are thus only slightly affected. Both the extrapolation scheme, which for $BaZrO_3$ is possible due to the small 5 atom cubic unit cell, and explicit electrostatic corrections have been considered in all papers that deal with formation energies. The corrections are expected to work well since the considered defects all have a localized charge distributions. Regarding the work on grain boundaries (Papers I-IV) no corrections were employed for the segregation energies. While these quantities are formation energy differences and should in principle include corrections, practical calculations using Eq. (5.37) involve only one supercell size and the errors are therefore expected to cancel.

5.3.2 Band gap problem

Formation energies calculated with local and semi-local functionals are subject to additional errors due to the band gap problem (see Section 5.1.3). For wide band gap materials the gap can be underestimated by several electron volts, which may lead to significant errors in the formation energies. However, it is actually not the size of the band gap that influence the formation energy and related properties but the position of the band edges and defect levels. Having only access to the correct band gap (e.g., from experiments) is therefore not sufficient, which is demonstrated schematically in Fig. 5.2. There is also the possibility that defect levels that should be located inside the band gap end up in the valence or conduction band, which could alter not only the formation energies but also the electronic character of the defects.

A straightforward approach to correct for these errors is simply to carry out the complete defect calculation with a method that treats the band gap more accurately, such as hybrid functionals. This approach quickly becomes computationally expensive and is limited to fairly small systems and structural relaxation is often very expensive. A common methodology is therefore to relax the defect structure using a local or semi-local functionals and then perform a static hybrid calculation with the relaxed structure. This procedure was considered in Papers VI and IX.

A different approach, which does not require explicit defect calculations with more demanding methods, is to apply a band gap correction directly to the formation energy in Eq. (5.34) [181, 182]. In this way, only one calculation beyond standard DFT is necessary in order to correct errors induced by the band gap problem. A difficulty with this method lies in the fact that it is not always obvious how

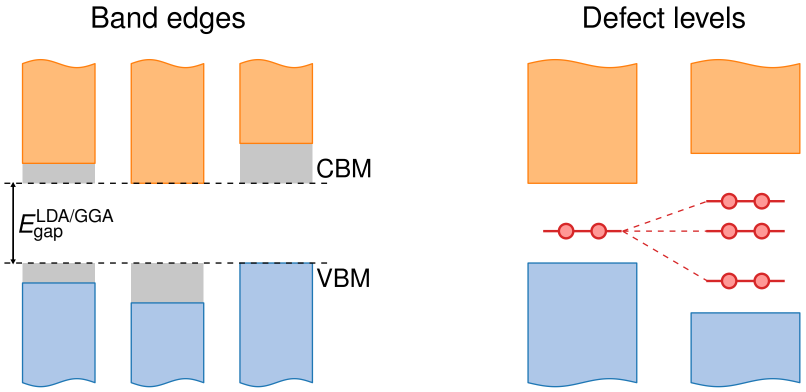

Figure 5.2: Schematic representation of the ambiguity that arise for the position of band edges (left panel) and defect levels (right panel) due to the band gap problem. Valence and conduction bands are represented by the blue and orange regions, respectively, while the grey shaded areas indicate band edge shifts.

defect levels follow band edges when band gaps open up and this information is not obtained from the ideal system (see Fig. 5.2). Within this context a key result of Paper IX is that the position of the oxygen vacancy level is well described already at the semi-local level and that the CTLs appear to be aligned (with respect to the vacuum level) for oxides in general. In the special case of fully ionized defects this correction scheme becomes much more simple. The conduction band and defect levels are then empty and only the shift of the VBM is of importance [183]. In this case the band gap correction to Eq. (5.34) is given by

$$E_{\mathrm{corr}}^{\mathrm{gap}}(q) = q\Delta\epsilon_{\mathrm{VBM}}, \tag{5.40}$$

where $\Delta\epsilon_{\mathrm{VBM}} = \epsilon_{\mathrm{VBM}} - \epsilon_{\mathrm{VBM}}^{\mathrm{DFT}}$ is the VBM shift. This correction was employed in Papers IV and VI with $\Delta\epsilon_{\mathrm{VBM}}$ being calculated from hybrid and G_0W_0 calculations.

5.4 Nuclear motion

The motion of the nuclei is often approached with the assumption that quantum mechanical effects are quite small and it is therefore reasonable to consider a classical treatment of the nuclei. Furthermore, the Hellmann-Feynman theorem [184] yields the following simple relation between the force exerted on a nucleus I and the total energy E of the ion-electron system

$$\boldsymbol{F}_I = -\frac{\partial E}{\partial \boldsymbol{R}_I}. \tag{5.41}$$

The forces can be used in many different contexts where ions are allowed to change position, such as in minimization schemes to find low energy structures or in Newton's equation of motion to study dynamical properties. The following two sections treat aspects of nuclear motion that have been considered in this thesis work and where forces play a major role.

5.4.1 Vibrational motion

Atomic forces are central to the description of vibrational motion in solid materials. This section gives a short introduction the methodology for computing the vibrational spectra and is a summary of more involved descriptions found in textbooks [185].

Since the potential energy depends on the ionic positions $\boldsymbol{R}$ it is possible to expand the energy around a set of coordinates $\tilde{\boldsymbol{R}}$ in terms of ionic displacements dR

$$V(\boldsymbol{R}) = V(\tilde{\boldsymbol{R}}) + \sum_{ki\alpha} \frac{\partial V(\tilde{\boldsymbol{R}})}{\partial R_{ki\alpha}} dR_{ki\alpha} + \frac{1}{2} \sum_{ki\alpha} \sum_{lj\beta} \frac{\partial^2 V(\tilde{\boldsymbol{R}})}{\partial R_{ki\alpha} \partial R_{lj\beta}} dR_{ki\alpha} dR_{lj\beta} + \dots, \tag{5.42}$$

where the indices kl, ij and $\alpha\beta$ sum over unit cells, atoms within the unit cell and cartesian coordinates, respectively. The zero order term in this expansion is a constant while the first-order term vanishes if the configuration represented by $\tilde{\boldsymbol{R}}$ corresponds to a minimum of the potential energy surface, and the second-order term is thus the first one of importance. The terms in the series become significantly more complex as the order increases and for many practical calculations where displacements are small the second-order term dominates. Considering only this term is referred to as the *harmonic approximation* and is often sufficient for describing the vibrational properties of materials. There are, however, certain properties such as thermal expansion and thermal transport that are not captured by this approximation and require consideration of the *anharmonic* third- and higher-order terms.

The second-order coefficients can be expressed in matrix form as the so-called *force constant matrix*

$$\Phi_{ki\alpha,lj\beta} = \frac{\partial^2 V(\tilde{\boldsymbol{R}})}{\partial R_{ki\alpha} \partial R_{lj\beta}} = -\frac{\partial F_{lj\beta}}{\partial R_{ki\alpha}}. \tag{5.43}$$

By considering the force constant matrix together with Newton's equations of motion and wavelike solutions it is possible to derive the eigenvalue problem

$$D(\boldsymbol{q})\boldsymbol{e}_{\boldsymbol{q}s} = \omega_{\boldsymbol{q}s}^2 \boldsymbol{e}_{\boldsymbol{q}s}, \tag{5.44}$$

where $\omega_{\boldsymbol{q}s}$ is the vibrational frequency of the mode with band index s and wave vector $\boldsymbol{q}$, $\boldsymbol{e}_{\boldsymbol{q}s}$ is the corresponding eigenvector, and $D(\boldsymbol{q})$ is the *dynamical matrix*.

The latter is obtained from the force constant matrix according to

$$D_{i\alpha,j\beta}(\boldsymbol{q}) = \frac{1}{\sqrt{M_i M_j}} \sum_k \Phi_{ki\alpha,0j\beta} \exp\left[-\mathrm{i}\boldsymbol{q} \cdot \left(\boldsymbol{R}_{ki} - \boldsymbol{R}_{0j}\right)\right]. \tag{5.45}$$

By solving the eigenvalue problem [Eq. (5.44)] for different $\boldsymbol{q}$ it is possible to obtain the complete vibrational spectrum. With this information it is then possible to study a variety of related properties, such the vibrational contribution to thermodynamic quantities (see Section 3.4).

5.4.2 Nudged elastic band method

As described in Chapter 4, when ions and polarons migrate from one site to the next they need to overcome a migration barrier. The configuration that corresponds to the top of the migration barrier is referred to as the transition state and is a saddle point on the energy landscape. This configuration is therefore difficult to find by standard minimization techniques whose purpose is to find local and global minima. A method that has become popular for finding the transition state is the nudged elastic band (NEB) method [186]. The approach here is to construct a minimum energy migration coordinate between the initial and final states that is represented by several intermediate configurations, or *images*, which are connected through springs. By constructing a tangent at each image and project out the corresponding force component, images are allowed to relax only in the perpendicular plane while remaining on the migration coordinate. A variant of this method is the climbing image NEB method [187] where the highest energy is not attached to the springs and can move freely along the migration coordinate. The saddle point can then be obtained by maximizing the energy of this image. These methods were used to compute adiabatic polaron migration barriers in Paper VII.

6

Summary of the papers

6.1 Papers I-IV: Space-charge formation at grain boundaries in $BaZrO_3$

As pointed out in Section 2.2, the low proton conductivity in polycrystalline $BaZrO_3$ is mainly due to the presence of space charges at grain boundaries, which impede transport across these interfaces. The aim with these four papers was to study this phenomenon and unravel the mechanisms behind space-charge formation from a theoretical point of view, by the means of first-principles calculations and thermodynamic modeling. Several different questions concerning space-charge formation are addressed, which range from fundamental physical aspects to more technical details. The main themes of the papers are the following: (i) do oxygen vacancies and protons segregate to the grain boundary and is this general for all grain boundaries in the material; (ii) is the vibrational contribution important when calculating segregation energies; (iii) why are grain boundaries more resistive in $BaZrO_3$ compared to $BaCeO_3$.

The first question is the topic of Papers I and II, where proton and oxygen vacancy segregation to four different stoichiometric tilt grain boundaries is considered. Three mirror-symmetric grain boundaries are under investigation in the first paper: $(111)[\bar{1}10]$, $(112)[\bar{1}10]$ and $(210)[001]$, where the second boundary is shown as an example in Fig. 6.1. The notation is such that the parenthesis represents the miller index of the grain boundary plane while the tilt axes is given within the square brackets. The $(210)[001]$ orientation was also considered in Paper II, however, the atomic structure was further optimized using rigid body translations that resulted in a non-symmetric configuration. The same methodology was employed in both papers. Segregation energies were calculated using Eq. (5.37) and space-

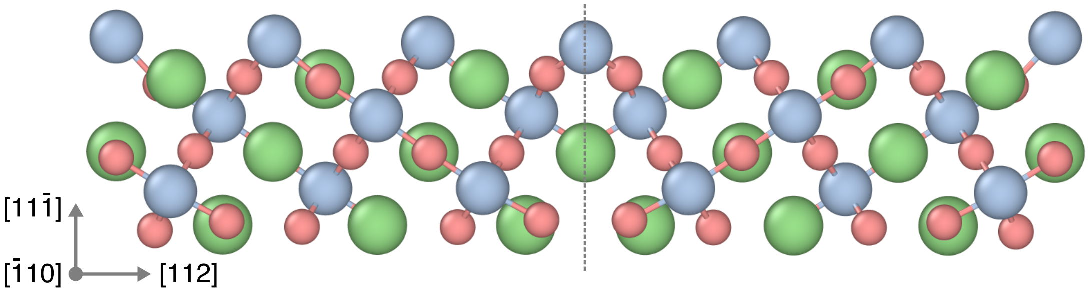

Figure 6.1: The atomic structure of the mirror-symmetric (112)[$\bar{1}$10] tilt grain boundary, where the grey dashed line marks the grain boundary plane. Green, blue and red atoms represent barium, zirconium, and oxygen, respectively.

charge modeling was performed as described in Section 3.6 using a layer-by-layer approach.

The most favorable vacancy segregation energies were found to be in the range −0.5 eV to −1.5 eV, while the corresponding range was −0.7 eV to −1.3 eV for protons. No direct trend was observed as some grain boundaries favored proton segregation while vacancies were more prone to segregate in others. Feeding these results into the space-charge model gave for dry conditions (where only oxygen vacancy segregation is considered) potential barriers between 0.2 V and 0.7 V, which are directly related to the strength of the segregation energies. This behavior was altered under hydrated conditions when protons were allowed to segregate. The space-charge potentials then became very similar and could be found within an interval of 0.6 V and 0.7 V at temperatures below 800 K for all grain boundaries. These results indicate that some potential barriers change quite significantly between dry and wet conditions while others remain unchanged. Both these scenarios have been observed experimentally although the differences in the measured potentials were smaller. Concentration profiles show that all grain boundaries were hydrated at low temperatures despite the fact that different boundaries favor different defects, which explain why the potential barriers become so similar. Protons thus appear to be the prime source to space-charge formation in wet atmospheres for temperatures below 800 K, which are typical conditions for applications that rely on proton conduction.

The second question is addressed in Paper III where first-principles phonon calculations where used to calculate segregation free energies in the (112)[$\bar{1}$10] grain boundary (Fig. 6.1). At this time, several acceptor dopants (Sc, Y, In, Gd) were also considered along with protons and oxygen vacancies. For protons, the vibrational contribution is very small and the segregation free energy is fairly constant at temperatures where protons remain in the material. For the vacancy, the addition of the phonon contribution leads to a positive segregation entropy, which further stabilizes the defect when temperature is increased. While this shifts the onset for hydration/dehydration of the GB core it does not change the conclusions of Papers I and II. For the dopants, on the other hand, the vibrational contribution is found to play a significant role. Segregation energies at zero Kelvin are found to correlate with the ionic radius, where the small (large) dopants display positive (negative) segregation energies. A similar trend is found for the segregation entropies. At high temperatures where dopants become mobile this leads to segregation free energies that are close to zero for all species. Dopant segregation is thus mainly driven by the attraction to the positively charged grain boundary and should be similar for all dopant species, which has also been observed experimentally. Hence, neglecting the vibrational contribution leads to the wrong conclusion that dopant segregation depends on the ionic radius. Furthermore, using these segregation free energies and allowing for dopants to segregate leads to a reduction in the space-charge potential by about 0.2 V, which is in agreement with experiments where samples were annealed at high temperatures.

The third and final question is treated in Paper IV, where formation and segregation protons and oxygen vacancies were studied for several different $BaZrO_3$ and $BaCeO_3$ grain boundaries. For a fair comparison of the two materials the grain boundaries need to be structurally similar. To this end the $(111)[\bar{1}10]$ and $(112)[\bar{1}10]$ grain boundaries from Papers I and III were considered for $BaZrO_3$ and analogous grain boundaries were then constructed for $BaCeO_3$. Furthermore, the hydration thermodynamics of the bulk is much more favorable in orthorhombic $BaCeO_3$ and this aspect was also taken into consideration. The DFT calculations imply that the energetics of oxygen vacancy formation and segregation are similar in the two materials. For protons, however, the materials behave differently where the segregation energy is found to be twice as negative in $BaZrO_3$. This leads to larger concentrations of protonic defects in the grain boundary cores at lower temperatures in humid environments for $BaZrO_3$. In turn, this results in space-charge potentials that are 0.1-0.3 V higher compared to those found for $BaCeO_3$ under the same conditions. Further analysis of proton formation energies revealed that they are all very similar in the grain boundaries of both materials and the difference in the segregation energies follows from that protons in the bulk region are more stable in $BaCeO_3$ compared to $BaZrO_3$. The reason for this can be explained by the local proton environments where the stronger hydrogen bonds found at grain boundaries and in the bulk phase of $BaCeO_3$ stabilize the proton. To conclude, the less resistive character of grain boundaries in $BaCeO_3$ stems from that the bulk phase of this material is more favorable for protons compared to the $BaZrO_3$ counterpart.

6.2 Paper V: Chemical expansion in $BaZrO_3$

This paper addresses chemical expansion in $BaZrO_3$, which in this context refers to the increase in volume that follows from the hydration of oxygen vacancies [Eq. (2.3)]. The study is performed from a defect point of view, where the size of protons and oxygen vacancies is used as a basis for describing the macroscopic chemical expansion. Protons and oxygen vacancies have been considered both as free defects and in association with several acceptor dopants (Ga, Sc, In, Y). Defect formation volumes have been quantified in terms of the defect induced strain tensor, which contain information about anisotropic distortions and thus provides a measure of both the *size* as well as the *shape* of defects. Moreover, the chemical expansion coefficient is given by the trace of the strain tensor and allows for a direct comparison with experimental data.

Strain tensors based on DFT calculations indicate that the formation of both protons and vacancies lead to anisotropic distortions and a net contraction of the lattice. The effect is smaller for the proton, which actually expands the lattice slightly along the Zr-O-Zr direction, and the net effect upon hydration is a volume expansion. The effects of dopant association are quite small and all corresponding expansion coefficients due to hydration are found within the range 0.4-0.6 per proton. While the calculated results appear to be slightly lower than what is found experimentally, an accurate quantitative assessment is not possible as there are major uncertainties in the experimental data. This is due to the actual proton concentration often differ from the nominal one and measurements of the former are usually either missing or not sufficiently accurate. Nevertheless, the qualitative agreement suggests that chemical expansion due to hydration follows from the size difference between protons and oxygen vacancies.

6.3 Papers VI and VII: Hole conductivity in $BaZrO_3$

While it is well established that acceptor-doped $BaZrO_3$ display hole conductivity at high temperatures in oxidizing environments, questions still remain concerning the origin of this behavior. Control over conductivity under different conditions is key in practical applications, which require an understanding of the different mechanisms at play. In these two papers we address two factors that determine the hole conductivity: the oxidation reaction [Eq. (2.5)] and hole polarons. Using DFT with LDA and GGAs is not sufficient here and an important aspect of these papers is to treat the shortcomings of local and semi-local functionals systematically.

Oxidation of oxygen vacancies is the main topic of Paper VI. This reaction describes the formation of holes and is therefore affected by the band gap problem (see Section 5.1.3). The issue is evident in the expression for the oxidation enthalpy, which depends on the position of the valence band maximum (VBM) as $\Delta H_{\mathrm{ox}} \propto -2\epsilon_{\mathrm{VBM}}$. To study how the description of the band gap affects modeling of the reaction we consider three different methods: DFT with both PBE and PBE0 as well as G_0W_0. The enthalpy was calculated explicitly with the two DFT methods while the VBM shift from G_0W_0 was applied as a correction to the PBE result [see Eq. (5.40)]. The latter approach is referred to as PBE+$\chi[G_0W_0]$. Additionally, the hydration of oxygen vacancies [Eq. (2.3)] was also considered within this context. However, the band gap problem was found not to be an issue in this case and all three methods predict consistent results for this reaction.

The calculated band gaps are 3.13 eV, 5.35 eV and 4.73 eV for PBE, PBE0 and G_0W_0 respectively. Experimental gaps are found in the range 4.8-5.3 eV, which indicates that both PBE0 and G_0W_0 predict reasonable gaps while PBE underestimate by about 40% as expected. Most of the increase in the band gaps is due to a shift of the VBM, which for PBE0 and G_0W_0 are -1.42 eV and -1.10 eV with respect to PBE. Due to the VBM dependence of ΔH_{ox} and the magnitude of these shifts, the description of the reaction changes drastically with an improved band gap. With PBE the reaction becomes exothermic with an enthalpy of -1.3 eV. Using PBE0 and PBE+$\chi[G_0W_0]$, on the other hand, lead to enthalpies of 1.5 eV and 0.9 eV, which correspond to an endothermic reaction. Further analysis using thermodynamic modeling showed that the qualitative difference between the methods has a huge impact on equilibrium defect concentrations. The exothermic nature of PBE leads to extremely large hole concentrations, which fully compensate acceptor dopants under dry conditions except at very low oxygen partial pressures. In wet atmospheres there is still a substantial amount of holes present that compensate about half of the dopant charge at low temperatures while protons compensate the remaining half. With PBE0 and PBE+$\chi[G_0W_0]$, however, oxygen vacancies become majority defects in dry atmospheres and holes dominate only at high temperatures and oxygen partial pressures. Additionally, almost complete hydration is obtained under wet conditions and the hole concentration is orders of magnitude lower than the proton concentration in this case. This latter scenario is in line with literature data as almost completely hydrated samples have been obtained experimentally under similar conditions.

While there is no experimental data available in the literature for the oxidation enthalpy of $BaZrO_3$ it is possible to relate this quantity to the activation energy for hole conduction, which have been measured by several different research groups. Such an assessment requires the hole mobility, which in turn depends on wether holes are delocalized or form localized polaronic states (see Section 4.2). Polaron formation also affects the oxidation enthalpy, which in this case corresponds to the reaction in Eq. (3.32), and can thus lead to different activation energies as well. To this end we study hole polaron formation and migration in $BaZrO_3$.

Modeling of polarons require certain considerations due to the self-interaction error of LDA and GGAs that favors charge delocalization (see Section 5.1.3). To address this problem we considered three different approaches: PBE+U, pSIC-PBE and and the hybrid functional HSE. The U parameter for PBE+U was determined based on the concept of piecewise linearity (see Section 5.1.3), which led to $U = 6.5\,\mathrm{eV}$. Similar results are obtained for all methods, which predict that polarons are stable and associated with a formation energy of -0.1 to $-0.2\,\mathrm{eV}$. The polaron mainly localizes on a single oxygen ion (see Fig. 3.2) and further investigation with an explicit yttrium acceptor show that yttrium act as a trap site with a trapping energy of about -0.1 eV. Polaron migration barriers were also calculated and found to be about 0.1 eV.

While polaron formation is energetically favorable, the rather small formation energies indicate that polarons will likely thermalize at higher temperatures and form band states. It is thus relevant to consider both band and polaron conduction mechanisms for calculating activation energies [see Eq. (4.11) and Eq. (4.12)]. Activation energies in the range 0.6-1.0 eV are obtained if a band hole mobility is considered together with the endothermic enthalpies of PBE0 and PBE+$\chi[G_0W_0]$. For polarons the corresponding activation energies are found to be within 0.4-0.8 eV. Both scenarios agree well with experimental data for Y-doped $BaZrO_3$ (0.6-1.1 eV) although band conduction fits slightly better. It is thus difficult to distinguish the hole character in the real samples. However, using an exothermic enthalpy as predicted by PBE the activation energies become negative with both mobility types. This is not sensible and the oxidation reaction must therefore be endothermic.

6.4 Paper VIII: Electronic defects in $BaTiO_{3-x}H_x$

In this paper we did a systematic investigation of the character of electronic carriers in $BaTiO_{3-x}H_x$ by combining first-principles calculations with inelastic neutron scattering (INS) techniques. For the excess electron that follows from hydride substitution of oxygen two different options are considered. It can either be promoted to conduction band and form a delocalized band state, or localize as a small polaron on a single titanium ion. In the latter scenario the electron localizes next to the hydride ion forming a bound polaron (see Fig. 3.2).

The energetics of the two states were determined by computing their respective formation energies. PBE+U was used capture localization, where U was chosen to fulfill piecewise linearity using the same procedure as in Paper VII. Two different supercell sizes were considered, 2×2×2 and 3×3×3, for which two slightly different U values were obtained (3.3 eV and 3.1 eV). Polaron formation was found to be favorable in the smaller supercell but not in the larger, which gives an indication to that the two charge carriers are present at different hydride concentrations. The associated formation energies are quite small, −60 meV and 120 meV, respectively.

The character of the electron in the real samples is determined indirectly by using INS techniques to measure the vibrational spectrum of hydrogen in the material. This approach was justified by first-principles phonon calculations, which show that the polaronic distortions around the hydride ion lead to significant shifts in the vibrational frequencies of hydrogen. The INS measurements were performed at 10 K using two samples with different hydrogen content. To assign the peaks in the measured spectra we used the more demanding HSE functional to calculate vibrational frequencies since hybrid functionals have been shown to predict the vibrational properties of pure $BaTiO_3$ more accurately than LDA and GGAs. Furthermore, we utilized the fact that hydrogen motion is decoupled from lattice vibrations and compute the hydrogen frequencies using a one particle harmonic potential method. The results indicate that excess electrons are mainly delocalized band states in both samples, however, polarons seem to appear when the amount of hydrogen in the material increases. To summarize, this study shows that INS together with first-principles modeling can be used to characterize electronic defects in oxyhydrides.

6.5 Paper IX: The oxygen vacancy

The oxygen vacancy is arguably the most important defect in oxides and many properties in these materials are associated with this defect. When formed intrinsically, the vacancy act as donor and can contribute with up to two electrons to the conduction band. The tendency to donate electrons depends on the position of the (+2/0) CTL (see Section 5.3) and a vacancy with a CTL close to (far from) the conduction band minimum is referred to as *shallow* (*deep*). The formation of an oxygen vacancy results in dangling bonds at the neighboring cations, which form the defect state. Since these cations differ between oxides and can exhibit either *s*-, *p*-, *d*-, or *f*-type character it is quite natural to assume that the behavior of the oxygen vacancy varies accordingly.

Here, however, we show using DFT that oxygen vacancies display the same properties in a large set of binary and ternary oxides. More specifically, the considered materials are charge transfer oxides where the valence bands derive from oxygen *p*-orbitals while the cations form the conduction bands. We find that when the oxide band structures are aligned the CTLs for all materials are found within ±0.6 eV while at the same time the corresponding band gaps vary between 3 and 10 eV. Since the CTL appears to be universal this indicates that it possible to identify the character of the vacancy (deep or shallow) directly from the band structure without an explicit treatment of the defect. Moreover, deep vacancies are found to behave as cavities where the predominantly s-like charge density is centered around the vacant site, regardless of surrounding cations.

Another important finding, which is of more technical concern, is that oxygen vacancies can be correctly classified as either deep or shallow based on calculations using semi-local functionals despite the inherent band gap problem. While the CTLs of shallow vacancies are found to follow the conduction band, those of deep vacancies do not and the absolute position of the latter is not changed when going from a semi-local description to a hybrid functional. At the semi-local level, however, it is not possible to classify the vacancy as deep or shallow from the position of the CTL since the band edges are misplaced. We show that there are several other quantities that also serve as predictors for the donor character, which are properly described with semi-local functionals. These are the *defect charge density*, the *relaxation behavior* and the *Kohn-Sham (KS) energy spectrum*. As described above, the charge density for deep vacancies is s-like and localized at the vacant site. This localization leads to different relaxed structures for the two charged states, a feature which is not observed for shallow vacancies. Finally, for deep vacancies there are localized KS levels within the band gap.

7

Conclusions and outlook

This thesis provides several new insights to the field of solid oxides (in particular for proton conducting ceramics), which can be divided into two categories. The first one concerns practical problems that prohibits acceptor-doped $BaZrO_3$ from becoming the superior proton conductor it has potential to be. The main issue is the resistive properties of grain boundaries in this material that have troubled scientists for almost two decades. While the material has been improved over the years, the origin of this phenomenon has not yet been fully understood and many advances have been achieved based on trial and error procedure. The work here provides more understanding of the mechanisms at play, i.e., the origin of space-charge formation, which can help as a guide for experimentalists in fabricating new better-performing materials. At this moment, the most important contribution is the comparison of $BaZrO_3$ and $BaCeO_3$, as most considered electrolyte materials at present are $BaZrO_3$-$BaCeO_3$ solid solutions. The fact that the bulk and *not* the grain boundaries causes the difference between the two materials is quite unexpected, which provides a new starting point for further work.

The other category concerns the theoretical methodology for describing these materials. As such, the work on hole conductivity has not primarily been done to address a certain issue as in the case of the space-charge effects and chemical expansion, but to introduce and develop theoretical tools for accurately describe electronic defects in oxide ion and proton conductors, for which $BaZrO_3$ acts as a model system. The motivation for these papers was not only to show how standard DFT modeling is not sufficient in this case but also to demonstrate how the more advanced methods such as DFT+U and hybrid functionals perform based on their parametrization. The importance of a proper choice of methods is demonstrated in the combined experimental and theoretical study of the oxyhydride in Paper VIII, for which a careful systematic assessment of these techniques provided both qualitative and quantitative agreement between the theoretical and experimental results. The last paper also falls into this category, as it provides a general understanding of oxygen vacancies in different oxides as well as how the inherent shortcomings of DFT with semi-local functionals can be circumvented when describing certain defect states.

Although the work presented here has provided a deeper understanding of space-charge formation, chemical expansion and defect modeling in general there is still room for improvements. These studies have generally been performed using rather simple systems that only provide qualitative agreement with experiments, with the exception of Paper VIII. Further insight to these processes will require more quantitative assessments, both from an experimental and a theoretical point of view.

For space-charge formation there are important aspects that remain unclear and deserve further analysis, many of which in one way or another are related to defect-defect interactions. In a real grain boundary, the energy landscape should change as more defects segregate and segregation energies should thus vary accordingly, and eventually there could be situations where they become positive. While this is to some extent already included in the space-charge model as the electrochemical potential depend on the electrostatic potential, many effects are not accounted for when only segregation of single defects is treated explicitly. Defect-dopant interactions in bulk have been shown to vary with dopant species [188, 189] and it is possible that a similar behavior is found also in grain boundaries. Moreover, the rather high defect core concentrations that are predicted by space-charge modeling are bound to impose significant strain that should affect segregation energies.

Strain effects were completely ignored in Paper I but to some extent addressed in Papers II-IV. This was done by prohibiting segregation to certain sites that were chosen based on defect relaxation behavior. For the $(112)[\bar{1}10]$ grain boundary the various treatments lead to different space-charge potentials in the hydrated regime, which show the importance of defect-defect interactions. While it is fairly straightforward to perform more quantitative theoretical modeling of individual grain boundaries little is gained from such a study if the grain boundary is not present in the real material. The atomic structure of grain boundaries in real samples is yet to be characterized and there is need for such assessments before there is much value in performing more elaborate modeling of these structures. For instance, the atomic structure of grain boundaries in $SrTiO_3$ has been identified using high-resolution transmission electron microscopy [190, 191] and the same approach should be applicable also for $BaZrO_3$.

For the hole conductivity, further insights also require more quantitative measures. Although the band gap is significantly improved with PBE0 and G_0W_0 and both predict an endothermic oxidation there is still a difference between the two methods. The VBM is 0.3 eV lower for PBE0 compared to PBE+$\chi[G_0W_0]$, which leads to an increase in the oxidation enthalpy of about 0.6 eV that reduces the hole concentration by one or several orders of magnitude (see Fig. 7 in Paper VI). The spread in the improved theoretical band gaps is as large as the experimental band gap range, and a more accurate prediction of hole concentrations therefore require a better assessment of the electronic structure with both theoretical and experimental techniques. The rather good agreement of the hole conductivity activation energies is to some extent due to the large scatter in the experimental data. A greater understanding would require more input from the experimental side so that materials are as similar as possible when comparing experimental and theoretical data. This will require information such as how changes in the microstructure as well as the presence of dopants and other defects affect the electronic structure. Additionally, experimental measurements of quantities such as the oxidation enthalpy and hole mobility for pristine $BaZrO_3$ would also be of great value for validating the theoretical results.

The oxyhydride perovskites have only been around for several years and many aspects of these materials still remain unknown. Practical applications for these materials are not yet available and most relevant questions are at moment of a more fundamental character. The most important one is undoubtedly the character of the hydride ion diffusion. While a few studies have set out to address this question no satisfactory explanation has still been provided for the diffusion mechanism. As these materials contain high concentrations of hydride ions, electrons, and oxygen vacancies the diffusion is most likely affected by the interplay between these species. A fundamental understanding of the defect chemistry is therefore imperative. Other interesting questions where the defect chemistry also play a major role are if oxyhydride phases can be found in simple perovskites beyond the titanates, and what is the solubility limit for hydrogen in different oxyhydrides.

Finally, for the oxygen vacancies a natural next step would be to investigate if the observed general behavior extends to more exotic materials, such as lanthanide oxides with open *f*-shells, layered 2D oxides and Mott insulators.

Acknowledgments

First of all, I would like to express my sincerest gratitude towards my main supervisor *Göran Wahnström*. His guidance and support throughout this Ph.D. project has been invaluable. I appreciate the fact that he has been very much involved in the daily work and for giving me the opportunity to attend a large number of international conferences and summer schools.

My assistant supervisor *Paul Erhart* also deserves a great deal of appreciation. He always finds time to answer my many questions and he has been crucial for my understanding of much of the work in this thesis.

I would also like to thank all present and former members of the MST group for contributing to a fun and stimulating working environment, where a few people need special mentioning: *Edit Helgee* and *Joakim Nyman* for helping me getting started when I joined the group as a master student as well as for putting a huge effort into the work on the grain boundary project; *Erik Jedvik Granhed* for a great collaboration on chemical expansion and the oxyhydrides; *Christopher Linderälv* for deep discussions about oxygen vacancies.

Several people outside MST also deserve credit. *Tor Svendsen Bjørheim* for inviting me to Oslo on numerous occasions. *Maths Karlsson* and his fellow group members for the collaboration on the oxyhydrides and other ongoing projects. *Alexander Stukowski* for spending his weekend in Gothenburg customizing OVITO to fit my specific needs.

Working and studying at Chalmers is not always a walk in the park and therefore I would especially like to thank two of my former classmates, *Emil* and *Nils*, which have been my fellow companions during my years at Chalmers. They have given me lots of fond memories from quiz nights and late nights on the pub. My friends from outside Chalmers also deserve credit for distracting me from work on a regular basis.

I would also like to express my gratitude towards my parents *Solvig* and *Mats* for all their love and support.

Finally, I thank *Magdalena*, *Frank* and *Stellan* for making our home a fun and happy place. I love you.

Bibliography

[1] J. D. Hunter, *Matplotlib: A 2D graphics environment*, Computing In Science & Engineering **9**, 90 (2007).

[2] A. Stukowski, *Visualization and analysis of atomistic simulation data with OVITO–the Open Visualization Tool*, Modelling and Simulation in Materials Science and Engineering **18**, 015012 (2010).

[3] Inkscape Project, *Inkscape 0.91*, 2015-01-28, https://inkscape.org.

[4] G. W. Crabtree, M. S. Dresselhaus, and M. V. Buchanan, *The hydrogen economy*, Physics Today **57**, 39 (2004).

[5] *Advances in Medium and High Temperature Solid Oxide Fuel Cell Technology*, Vol. 574 of *CISM International Centre for Mechanical Sciences*, edited by M. Boaro and A. A. Salvatore (Springer International Publishing, Cham, 2017).

[6] M. Stoukides, *Solid-Electrolyte Membrane Reactors: Current Experience and Future Outlook*, Catalysis Reviews **42**, 1 (2000).

[7] H. Iwahara, Y. Asakura, K. Katahira, and M. Tanaka, *Prospect of hydrogen technology using proton-conducting ceramics*, Solid State Ionics **168**, 299 (2004).

[8] L. Carrette, K. A. Friedrich, and U. Stimming, *Fuel Cells – Fundamentals and Applications*, Fuel Cells **1**, 5 (2001).

[9] A. J. Jacobson, *Materials for Solid Oxide Fuel Cells*, Chemistry of Materials **22**, 660 (2009).

[10] L. Malavasi, C. A. J. Fisher, and M. S. Islam, *Oxide-ion and proton conducting electrolyte materials for clean energy applications: structural and mechanistic features*, Chemical Society Reviews **39**, 4370 (2010).

[11] E. D. Wachsman and K. T. Lee, *Lowering the Temperature of Solid Oxide Fuel Cells*, Science **334**, 935 (2011).

[12] E. Fabbri, L. Bi, D. Pergolesi, and E. Traversa, *Towards the Next Generation of Solid Oxide Fuel Cells Operating Below 600 °C with Chemically Stable Proton-Conducting Electrolytes*, Advanced Materials **24**, 195 (2012).

[13] K. D. Kreuer, *Proton-Conducting Oxides*, Annual Review of Materials Research **33**, 333 (2003).

[14] T. Norby, in *Perovskite Oxide for Solid Oxide Fuel Cells*, *Fuel Cells and Hydrogen Energy*, edited by T. Ishihara (Springer US, Boston, Massachusetts, 2009), pp. 217–241.

[15] *Proton-Conducting Ceramics: From Fundamentals to Applied Research*, edited by M. Marrony (Pan Stanford, Boca Raton, 2015).

[16] T. Takahashi and H. Iwahara, *Solid-state ionics: protonic conduction in perovskite type oxide solid solutions*, Revue de Chimie Minérale **17(4)**, 243 (1980).

[17] C. Duan, J. Tong, M. Shang, S. Nikodemski, M. Sanders, S. Ricote, A. Almansoori, and R. O'Hayre, *Readily processed protonic ceramic fuel cells with high performance at low temperatures*, Science **349**, 1321 (2015).

[18] S. H. Morejudo, R. Zanón, S. Escolástico, I. Yuste-Tirados, H. Malerød-Fjeld, P. K. Vestre, W. G. Coors, A. Martínez, T. Norby, J. M. Serra, and C. Kjølseth, *Direct conversion of methane to aromatics in a catalytic co-ionic membrane reactor*, Science **353**, 563 (2016).

[19] A. Vourros, V. Kyriakou, I. Garagounis, E. Vasileiou, and M. Stoukides, *Chemical reactors with high temperature proton conductors as a main component: Progress in the past decade*, Solid State Ionics, **In Press**, (2017), doi: 10.1016/j.ssi.2017.02.019.

[20] C. Sun and U. Stimming, *Recent anode advances in solid oxide fuel cells*, Journal of Power Sources **171**, 247 (2007).

[21] D. J. L. Brett, A. Atkinson, N. P. Brandon, and S. J. Skinner, *Intermediate temperature solid oxide fuel cells*, Chemical Society Reviews **37**, 1568 (2008).

[22] A. Orera and P. R. Slater, *New Chemical Systems for Solid Oxide Fuel Cells*, Chemistry of Materials **22**, 675 (2009).

[23] A. Klein, *Transparent Conducting Oxides: Electronic Structure–Property Relationship from Photoelectron Spectroscopy with in situ Sample Preparation*, Journal of the American Ceramic Society **96**, 331 (2013).

[24] G. Busca, L. Lietti, G. Ramis, and F. Berti, *Chemical and mechanistic aspects of the selective catalytic reduction of NO_x by ammonia over oxide catalysts: A review*, Applied Catalysis B: Environmental **18**, 1 (1998).

[25] R. A. B. Devine, J.-P. Duraud, and E. Dooryhée, *Structure and imperfections in amorphous and crystalline silicon dioxide* (Wiley, Chichester, 2000).

[26] M. E. Lines and A. M. Glass, *Principles and Applications of Ferroelectrics and Related Materials* (Oxford University Press, New York, 1977).

[27] K. M. Rabe, C. H. Ahn, and J.-M. Triscone, *Physics of Ferroelectrics: A Modern Perspective* (Springer Science & Business Media, Berlin Heidelberg, 2007).

[28] V. V. Kharton, F. M. B. Marques, and A. Atkinson, *Transport properties of solid oxide electrolyte ceramics: a brief review*, Solid State Ionics **174**, 135 (2004).

[29] J. Sunarso, S. Baumann, J. M. Serra, W. A. Meulenberg, S. Liu, Y. S. Lin, and J. C. Diniz da Costa, *Mixed ionic–electronic conducting (MIEC) ceramic-based membranes for oxygen separation*, Journal of Membrane Science **320**, 13 (2008).

[30] C. S. Koonce, M. L. Cohen, J. F. Schooley, W. R. Hosler, and E. R. Pfeiffer, *Superconducting Transition Temperatures of Semiconducting $SrTiO_3$*, Physical Review **163**, 380 (1967).

[31] T. D. Thanh, A. Koma, and S. Tanaka, *Superconductivity in the $BaPb_{1-x}$ Bi_x O_3 system*, Applied physics **22**, 205 (1980).

[32] R. J. Cava, B. Batlogg, R. B. van Dover, D. W. Murphy, S. Sunshine, T. Siegrist, J. P. Remeika, E. A. Rietman, S. Zahurak, and G. P. Espinosa, *Bulk superconductivity at 91 K in single-phase oxygen-deficient perovskite $Ba_2YCu_3O_{9-\delta}$*, Physical Review Letters **58**, 1676 (1987).

[33] G. H. Jonker and J. H. Van Santen, *Ferromagnetic compounds of manganese with perovskite structure*, Physica **16**, 337 (1950).

[34] R. M. Kusters, J. Singleton, D. A. Keen, R. McGreevy, and W. Hayes, *Magnetoresistance measurements on the magnetic semiconductor $Nd_{0.5}Pb_{0.5}MnO_3$*, Physica B: Condensed Matter **155**, 362 (1989).

[35] R. von Helmolt, J. Wecker, B. Holzapfel, L. Schultz, and K. Samwer, *Giant negative magnetoresistance in perovskitelike* $La_{2/3}Ba_{1/3}MnO_x$ *ferromagnetic films*, Physical Review Letters **71**, 2331 (1993).

[36] A. M. Glazer, *The classification of tilted octahedra in perovskites*, Acta Crystallographica Section B Structural Crystallography and Crystal Chemistry **28**, 3384 (1972).

[37] V. M. Goldschmidt, *Die Gesetze der Krystallochemie*, Naturwissenschaften **14**, 477 (1926).

[38] H. Iwahara, T. Esaka, H. Uchida, and N. Maeda, *Proton conduction in sintered oxides and its application to steam electrolysis for hydrogen production*, Solid State Ionics **3–4**, 359 (1981).

[39] H. Iwahara, H. Uchida, K. Ono, and K. Ogaki, *Proton Conduction in Sintered Oxides Based on* $BaCeO_3$, Journal of The Electrochemical Society **135**, 529 (1988).

[40] H. Iwahara, T. Yajima, T. Hibino, K. Ozaki, and H. Suzuki, *Protonic conduction in calcium, strontium and barium zirconates*, Solid State Ionics **61**, 65 (1993).

[41] A. S. Nowick and Y. Du, *High-temperature protonic conductors with perovskite-related structures*, Solid State Ionics **77**, 137 (1995).

[42] Y. Larring and T. Norby, *Protons in* $LaErO_3$, Solid State Ionics **70**, 305 (1994).

[43] T. Norby and Y. Larring, *Concentration and transport of protons in oxides*, Current Opinion in Solid State and Materials Science **2**, 593 (1997).

[44] T. He, K. Kreuer, Y. Baikov, and J. Maier, *Impedance spectroscopic study of thermodynamics and kinetics of a Gd-doped* $BaCeO_3$ *single crystal*, Solid State Ionics **95**, 301 (1997).

[45] K. Kreuer, *Aspects of the formation and mobility of protonic charge carriers and the stability of perovskite-type oxides*, Solid State Ionics **125**, 285 (1999).

[46] K. Kreuer, S. Adams, W. Münch, A. Fuchs, U. Klock, and J. Maier, *Proton conducting alkaline earth zirconates and titanates for high drain electrochemical applications*, Solid State Ionics **145**, 295 (2001).

[47] F. A. Kröger and H. J. Vink, in *Solid State Physics*, edited by F. Seitz and D. Turnbull (Academic Press, New York, 1956), Vol. 3, pp. 307–435.

[48] A. Løken, S. W. Saeed, M. N. Getz, X. Liu, and T. S. Bjørheim, *Alkali metals as efficient A-site acceptor dopants in proton conducting* $BaZrO_3$, Journal of Materials Chemistry A **4**, 9229 (2016).

[49] C. Hiraiwa, D. Han, A. Kuramitsu, A. Kuwabara, H. Takeuchi, M. Majima, and T. Uda, *Chemical Expansion and Change in Lattice Constant of Y-Doped* $BaZrO_3$ *by Hydration/Dehydration Reaction and Final Heat-Treating Temperature*, Journal of the American Ceramic Society **96**, 879 (2013).

[50] A. K. E. Andersson, S. M. Selbach, C. S. Knee, and T. Grande, *Chemical Expansion Due to Hydration of Proton-Conducting Perovskite Oxide Ceramics*, Journal of the American Ceramic Society **97**, 2654 (2014).

[51] R. Sažinas, M.-A. Einarsrud, and T. Grande, *Toughening of Y-doped* $BaZrO_3$ *proton conducting electrolytes by hydration*, Journal of Materials Chemistry A **5**, 5846 (2017).

[52] H. G. Bohn and T. Schober, *Electrical Conductivity of the High-Temperature Proton Conductor* $BaZr_{0.9}Y_{0.1}O_{2.95}$, Journal of the American Ceramic Society **83**, 768 (2000).

[53] W. Wang and A. V. Virkar, *Ionic and electron-hole conduction in* $BaZr_{0.93}Y_{0.07}O_{3-\delta}$ *by 4-probe dc measurements*, Journal of Power Sources **142**, 1 (2005).

[54] K. Nomura and H. Kageyama, *Transport properties of* $BaZr_{0.8}Y_{0.2}O_{3-\delta}$ *perovskite*, Solid State Ionics **178**, 661 (2007).

[55] G. Gregori, R. Merkle, and J. Maier, *Ion conduction and redistribution at grain boundaries in oxide systems*, Progress in Materials Science, **In Press**, (2017), doi: 10.1016/j.pmatsci.2017.04.009.

[56] F. Iguchi, N. Sata, and H. Yugami, *Proton transport properties at the grain boundary of barium zirconate based proton conductors for intermediate temperature operating SOFC*, Journal of Materials Chemistry **20**, 6265 (2010).

[57] F. Iguchi, T. Yamada, N. Sata, T. Tsurui, and H. Yugami, *The influence of grain structures on the electrical conductivity of a* $BaZr_{0.95}Y_{0.05}O_3$ *proton conductor*, Solid State Ionics **177**, 2381 (2006).

[58] P. Babilo, T. Uda, and S. M. Haile, *Processing of yttrium-doped barium zirconate for high proton conductivity*, Journal of Materials Research **22**, 1322 (2007).

[59] M. Shirpour, R. Merkle, C. T. Lin, and J. Maier, *Nonlinear electrical grain boundary properties in proton conducting Y–*$BaZrO_3$ *supporting the space charge depletion model*, Physical Chemistry Chemical Physics **14**, 730 (2011).

[60] F. Iguchi, T. Tsurui, N. Sata, Y. Nagao, and H. Yugami, *The relationship between chemical composition distributions and specific grain boundary conductivity in Y-doped* $BaZrO_3$ *proton conductors*, Solid State Ionics **180**, 563 (2009).

[61] P. I. Dahl, H. L. Lein, Y. Yu, J. Tolchard, T. Grande, M.-A. Einarsrud, C. Kjølseth, T. Norby, and R. Haugsrud, *Microstructural characterization and electrical properties of spray pyrolyzed conventionally sintered or hot-pressed* $BaZrO_3$ *and* $BaZr_{0.9}Y_{0.1}O_{3-\delta}$, Solid State Ionics **182**, 32 (2011).

[62] M. Shirpour, R. Merkle, and J. Maier, *Space charge depletion in grain boundaries of* $BaZrO_3$ *proton conductors*, Solid State Ionics **225**, 304 (2012).

[63] D.-H. Kim, B.-K. Kim, and Y.-C. Kim, *Energy barriers for proton migration in yttrium-doped barium zirconate super cell with* $\Sigma 5$ *(310)/[001] tilt grain boundary*, Solid State Ionics **213**, 18 (2012).

[64] J.-H. Yang, D.-H. Kim, B.-K. Kim, and Y.-C. Kim, *High activation energy for proton migration at tilt grain boundary in barium zirconate*, Solid State Ionics **252**, 126 (2013).

[65] J.-H. Yang, B.-K. Kim, and Y.-C. Kim, *Theoretical Analysis for Proton Conductivity at* $\Sigma 3$ *Tilt Grain Boundary of Barium Cerate*, Journal of Nanoscience and Nanotechnology **15**, 8584 (2015).

[66] C. Kjølseth, H. Fjeld, Ø. Prytz, P. I. Dahl, C. Estournès, R. Haugsrud, and T. Norby, *Space-charge theory applied to the grain boundary impedance of proton conducting* $BaZr_{0.9}Y_{0.1}O_{3-\delta}$, Solid State Ionics **181**, 268 (2010).

[67] C.-T. Chen, C. E. Danel, and S. Kim, *On the origin of the blocking effect of grain-boundaries on proton transport in yttrium-doped barium zirconates*, Journal of Materials Chemistry **21**, 5435 (2011).

[68] F. Iguchi, C.-T. Chen, H. Yugami, and S. Kim, *Direct evidence of potential barriers at grain boundaries in Y-doped* $BaZrO_3$ *from dc-bias dependence measurements*, Journal of Materials Chemistry **21**, 16517 (2011).

[69] M. Shirpour, B. Rahmati, W. Sigle, P. A. van Aken, R. Merkle, and J. Maier, *Dopant Segregation and Space Charge Effects in Proton-Conducting* $BaZrO_3$ *Perovskites*, The Journal of Physical Chemistry C **116**, 2453 (2012).

[70] M. Shirpour, R. Merkle, and J. Maier, *Evidence for space charge effects in Y-doped $BaZrO_3$ from reduction experiments*, Solid State Ionics **216**, 1 (2012).

[71] D. R. Clark, H. Zhu, D. R. Diercks, S. Ricote, R. J. Kee, A. Almansoori, B. P. Gorman, and R. P. O'Hayre, *Probing Grain-Boundary Chemistry and Electronic Structure in Proton-Conducting Oxides by Atom Probe Tomography*, Nano Letters **16**, 6924 (2016).

[72] J. B. Nyman, E. E. Helgee, and G. Wahnström, *Oxygen vacancy segregation and space-charge effects in grain boundaries of dry and hydrated $BaZrO_3$*, Applied Physics Letters **100**, 061903 (2012).

[73] J. M. Polfus, K. Toyoura, F. Oba, I. Tanaka, and R. Haugsrud, *Defect chemistry of a $BaZrO_3$ $\Sigma3$ (111) grain boundary by first principles calculations and space–charge theory*, Physical Chemistry Chemical Physics **14**, 12339 (2012).

[74] J.-S. Kim, J.-H. Yang, B.-K. Kim, and Y.-C. Kim, *Study of $\Sigma3$ $BaZrO_3$ (210)[001] tilt grain boundaries using density functional theory and a space charge layer model*, Journal of the Ceramic Society of Japan **123**, 245 (2015).

[75] J.-H. Yang, B.-K. Kim, and Y.-C. Kim, *Calculation of proton conductivity at the tilt grain boundary of barium zirconate using density functional theory*, Solid State Ionics **279**, 60 (2015).

[76] J.-S. Kim and Y.-C. Kim, *Proton Conduction in Nonstoichiometric $\Sigma3$ $BaZrO_3$ (210)[001] Tilt Grain Boundary Using Density Functional Theory*, Journal of the Korean Ceramic Society **53**, 301 (2016).

[77] R. A. De Souza, *The formation of equilibrium space-charge zones at grain boundaries in the perovskite oxide $SrTiO_3$*, Physical Chemistry Chemical Physics **11**, 9939 (2009).

[78] C.-T. Chen, S. K. Kim, M. Ibbotson, A. Yeung, and S. Kim, *Thermionic emission of protons across a grain boundary in 5 mol% Y-doped $SrZrO_3$, a hydrogen pump*, International Journal of Hydrogen Energy **37**, 12432 (2012).

[79] H. J. Park and S. Kim, *Space Charge Effects on the Interfacial Conduction in Sr-Doped Lanthanum Gallates: A Quantitative Analysis*, The Journal of Physical Chemistry C **111**, 14903 (2007).

[80] X. Guo and R. Waser, *Electrical properties of the grain boundaries of oxygen ion conductors: Acceptor-doped zirconia and ceria*, Progress in Materials Science **51**, 151 (2006).

[81] T. S. Bjørheim, M. Arrigoni, S. W. Saeed, E. Kotomin, and J. Maier, *Surface Segregation Entropy of Protons and Oxygen Vacancies in* $BaZrO_3$, Chemistry of Materials **28**, 1363 (2016).

[82] J. M. Polfus, T. S. Bjørheim, T. Norby, and R. Bredesen, *Surface defect chemistry of Y-substituted and hydrated* $BaZrO_3$ *with subsurface space-charge regions*, Journal of Materials Chemistry A **4**, 7437 (2016).

[83] J. M. Polfus, T. Norby, and R. Bredesen, *Proton segregation and space-charge at the* $BaZrO_3$ *(001)/MgO (001) heterointerface*, Solid State Ionics **297**, 77 (2016).

[84] J.-S. Kim and Y.-C. Kim, *Equilibrium crystal shape of* $BaZrO_3$ *and space charge formation in the (011) surface by using ab-initio thermodynamics*, Journal of the Korean Physical Society **70**, 75 (2017).

[85] S. Ricote, N. Bonanos, and G. Caboche, *Water vapour solubility and conductivity study of the proton conductor* $BaCe_{0.9-x}Zr_xY_{0.1}O_{3-\delta}$, Solid State Ionics **180**, 990 (2009).

[86] P. Babilo and S. M. Haile, *Enhanced Sintering of Yttrium-Doped Barium Zirconate by Addition of ZnO*, Journal of the American Ceramic Society **88**, 2362 (2005).

[87] S. Ricote, N. Bonanos, A. Manerbino, N. P. Sullivan, and W. G. Coors, *Effects of the fabrication process on the grain-boundary resistance in* $BaZr_{0.9}Y_{0.1}O_{3-\delta}$, Journal of Materials Chemistry A **2**, 16107 (2014).

[88] S. B. C. Duval, P. Holtappels, U. F. Vogt, E. Pomjakushina, K. Conder, U. Stimming, and T. Graule, *Electrical conductivity of the proton conductor* $BaZr_{0.9}Y_{0.1}O_{3-\delta}$ *obtained by high temperature annealing*, Solid State Ionics **178**, 1437 (2007).

[89] M. Shirpour, G. Gregori, L. Houben, R. Merkle, and J. Maier, *High spatially resolved cation concentration profile at the grain boundaries of Sc-doped* $BaZrO_3$, Solid State Ionics **262**, 860 (2014).

[90] K. Bae, D. Y. Jang, H. J. Choi, D. Kim, J. Hong, B.-K. Kim, J.-H. Lee, J.-W. Son, and J. H. Shim, *Demonstrating the potential of yttrium-doped barium zirconate electrolyte for high-performance fuel cells*, Nature Communications **8**, 14553 (2017).

[91] M. A. Hayward, E. J. Cussen, J. B. Claridge, M. Bieringer, M. J. Rosseinsky, C. J. Kiely, S. J. Blundell, I. M. Marshall, and F. L. Pratt, *The Hydride Anion*

in an Extended Transition Metal Oxide Array: $LaSrCoO_3H_{0.7}$, Science **295**, 1882 (2002).

[92] Y. Kobayashi, O. J. Hernandez, T. Sakaguchi, T. Yajima, T. Roisnel, Y. Tsujimoto, M. Morita, Y. Noda, Y. Mogami, A. Kitada, M. Ohkura, S. Hosokawa, Z. Li, K. Hayashi, Y. Kusano, J. e. Kim, N. Tsuji, A. Fujiwara, Y. Matsushita, K. Yoshimura, K. Takegoshi, M. Inoue, M. Takano, and H. Kageyama, *An oxyhydride of $BaTiO_3$ exhibiting hydride exchange and electronic conductivity*, Nature Materials **11**, 507 (2012).

[93] T. Sakaguchi, Y. Kobayashi, T. Yajima, M. Ohkura, C. Tassel, F. Takeiri, S. Mitsuoka, H. Ohkubo, T. Yamamoto, J. e. Kim, N. Tsuji, A. Fujihara, Y. Matsushita, J. Hester, M. Avdeev, K. Ohoyama, and H. Kageyama, *Oxyhydrides of $(Ca,Sr,Ba)TiO_3$ Perovskite Solid Solutions*, Inorganic Chemistry **51**, 11371 (2012).

[94] T. Yajima, A. Kitada, Y. Kobayashi, T. Sakaguchi, G. Bouilly, S. Kasahara, T. Terashima, M. Takano, and H. Kageyama, *Epitaxial Thin Films of $ATiO_{3-x}H_x$ (A = Ba, Sr, Ca) with Metallic Conductivity*, J. Am. Chem. Soc. **134**, 8782 (2012).

[95] G. Bouilly, T. Yajima, T. Terashima, W. Yoshimune, K. Nakano, C. Tassel, Y. Kususe, K. Fujita, K. Tanaka, T. Yamamoto, Y. Kobayashi, and H. Kageyama, *Electrical Properties of Epitaxial Thin Films of Oxyhydrides $ATiO_{3-x}H_x$ (A = Ba and Sr)*, Chemistry of Materials **27**, 6354 (2015).

[96] T. Yajima, F. Takeiri, K. Aidzu, H. Akamatsu, K. Fujita, W. Yoshimune, M. Ohkura, S. Lei, V. Gopalan, K. Tanaka, C. M. Brown, M. A. Green, T. Yamamoto, Y. Kobayashi, and H. Kageyama, *A labile hydride strategy for the synthesis of heavily nitridized $BaTiO_3$*, Nature Chemistry **7**, 1017 (2015).

[97] Y. Iwazaki, T. Suzuki, and S. Tsuneyuki, *Negatively charged hydrogen at oxygen-vacancy sites in $BaTiO_3$: Density-functional calculation*, Journal of Applied Physics **108**, 083705 (2010).

[98] J. Zhang, G. Gou, and B. Pan, *Study of Phase Stability and Hydride Diffusion Mechanism of $BaTiO_3$ Oxyhydride from First-Principles*, Journal of Physical Chemistry C **118**, 17254 (2014).

[99] X. Liu, T. S. Bjørheim, and R. Haugsrud, *Formation and migration of hydride ions in $BaTiO_{3-x}H_x$ oxyhydride*, Journal of Materials Chemistry A **5**, 1050 (2017).

[100] G. Kobayashi, Y. Hinuma, S. Matsuoka, A. Watanabe, M. Iqbal, M. Hirayama, M. Yonemura, T. Kamiyama, I. Tanaka, and R. Kanno, *Pure H-conduction in oxyhydrides*, Science **351**, 1314 (2016).

[101] S. Yamaguchi, *Large, soft, and polarizable hydride ions sneak around in an oxyhydride*, Science **351**, 1262 (2016).

[102] C. Kittel, *Introduction to Solid State Physics*, 8th ed. (John Wiley & Sons, Hoboken, New Jersey, 2005).

[103] H. Fröhlich, H. Pelzer, and S. Zienau, *XX. Properties of slow electrons in polar materials*, The London, Edinburgh, and Dublin Philosophical Magazine and Journal of Science **41**, 221 (1950).

[104] T. Holstein, *Studies of polaron motion*, Annals of Physics **8**, 325 (1959).

[105] J. T. Devreese, *Polarons in Ionic Crystals and Polar Semiconductors* (North-Holland Publishing Company, Amsterdam, Netherlands, 1972).

[106] T. S. Bjørheim, E. A. Kotomin, and J. Maier, *Hydration entropy of* $BaZrO_3$ *from first principles phonon calculations*, Journal of Materials Chemistry A **3**, 7639 (2015).

[107] P. Ágoston and K. Albe, *Formation entropies of intrinsic point defects in cubic* In_2O_3 *from first-principles density functional theory calculations*, Physical Chemistry Chemical Physics **11**, 3226 (2009).

[108] J. Maier, *Physical Chemistry of Ionic Materials: Ions and Electrons in Solids* (John Wiley & Sons, Chichester, West Sussex, 2004).

[109] R. A. De Souza, Z. A. Munir, S. Kim, and M. Martin, *Defect chemistry of grain boundaries in proton-conducting solid oxides*, Solid State Ionics **196**, 1 (2011).

[110] Y. Yamazaki, F. Blanc, Y. Okuyama, L. Buannic, J. C. Lucio-Vega, C. P. Grey, and S. M. Haile, *Proton trapping in yttrium-doped barium zirconate*, Nature Materials **12**, 647 (2013).

[111] H. Böttger and V. V. Bryksin, *Hopping Conduction in Solids* (VCH Verlagsgesellschaft, Weinheim, 1985).

[112] D. M. Smyth, *The Defect Chemistry of Metal Oxides* (Oxford University Press, New York, 2000).

[113] A. Einstein, *Über die von der molekularkinetischen Theorie der Wärme geforderte Bewegung von in ruhenden Flüssigkeiten suspendierten Teilchen*, Annalen der Physik **322**, 549 (1905).

[114] R. A. De Souza, *Oxygen Diffusion in $SrTiO_3$ and Related Perovskite Oxides*, Advanced Functional Materials **25**, 6326 (2015).

[115] K. D. Kreuer, *Proton Conductivity: Materials and Applications*, Chemistry of Materials **8**, 610 (1996).

[116] P. G. Sundell, M. E. Björketun, and G. Wahnström, *Density-functional calculations of prefactors and activation energies for H diffusion in $BaZrO_3$*, Physical Review B **76**, 094301 (2007).

[117] M. E. Björketun, P. G. Sundell, and G. Wahnström, *Effect of acceptor dopants on the proton mobility in $BaZrO_3$: A density functional investigation*, Physical Review B **76**, 054307 (2007).

[118] M. Born and R. Oppenheimer, *Zur Quantentheorie der Molekeln*, Annalen der Physik **389**, 457 (1927).

[119] W. Kohn, *Nobel Lecture: Electronic structure of matter—wave functions and density functionals*, Reviews of Modern Physics **71**, 1253 (1999).

[120] R. M. Martin, *Electronic Structure: Basic Theory and Practical Methods* (Cambridge University Press, Cambridge, 2004).

[121] J. Kohanoff, *Electronic Structure Calculations for Solids and Molecules: Theory and Computational Methods* (Cambridge University Press, Cambridge, 2006).

[122] K. Capelle, *A bird's-eye view of density-functional theory*, Brazilian Journal of Physics **36**, 1318 (2006).

[123] P. Hohenberg and W. Kohn, *Inhomogeneous Electron Gas*, Physical Review **136**, B864 (1964).

[124] W. Kohn and L. J. Sham, *Self-Consistent Equations Including Exchange and Correlation Effects*, Physical Review **140**, A1133 (1965).

[125] D. M. Ceperley and B. J. Alder, *Ground State of the Electron Gas by a Stochastic Method*, Physical Review Letters **45**, 566 (1980).

[126] M. G. Medvedev, I. S. Bushmarinov, J. Sun, J. P. Perdew, and K. A. Lyssenko, *Density functional theory is straying from the path toward the exact functional*, Science **355**, 49 (2017).

[127] J. P. Perdew, K. Burke, and M. Ernzerhof, *Generalized Gradient Approximation Made Simple*, Physical Review Letters **77**, 3865 (1996).

[128] M. Dion, H. Rydberg, E. Schröder, D. C. Langreth, and B. I. Lundqvist, *Van der Waals Density Functional for General Geometries*, Physical Review Letters **92**, 246401 (2004).

[129] K. Berland and P. Hyldgaard, *Exchange functional that tests the robustness of the plasmon description of the van der Waals density functional*, Physical Review B **89**, 035412 (2014).

[130] K. Berland, C. A. Arter, V. R. Cooper, K. Lee, B. I. Lundqvist, E. Schröder, T. Thonhauser, and P. Hyldgaard, *van der Waals density functionals built upon the electron-gas tradition: Facing the challenge of competing interactions*, The Journal of Chemical Physics **140**, 18A539 (2014).

[131] L. Gharaee, P. Erhart, and P. Hyldgaard, *Finite-temperature properties of nonmagnetic transition metals: Comparison of the performance of constraint-based semilocal and nonlocal functionals*, Physical Review B **95**, 085147 (2017).

[132] P. Mori-Sánchez, A. J. Cohen, and W. Yang, *Localization and Delocalization Errors in Density Functional Theory and Implications for Band-Gap Prediction*, Physical Review Letters **100**, 146401 (2008).

[133] A. J. Cohen, P. Mori-Sánchez, and W. Yang, *Fractional charge perspective on the band gap in density-functional theory*, Physical Review B **77**, 115123 (2008).

[134] J. P. Perdew, R. G. Parr, M. Levy, and J. L. Balduz, *Density-Functional Theory for Fractional Particle Number: Derivative Discontinuities of the Energy*, Physical Review Letters **49**, 1691 (1982).

[135] J. P. Perdew and M. Levy, *Physical Content of the Exact Kohn-Sham Orbital Energies: Band Gaps and Derivative Discontinuities*, Physical Review Letters **51**, 1884 (1983).

[136] L. J. Sham and M. Schlüter, *Density-Functional Theory of the Energy Gap*, Physical Review Letters **51**, 1888 (1983).

[137] R. W. Godby, M. Schlüter, and L. J. Sham, *Accurate Exchange-Correlation Potential for Silicon and Its Discontinuity on Addition of an Electron*, Physical Review Letters **56**, 2415 (1986).

[138] V. I. Anisimov, J. Zaanen, and O. K. Andersen, *Band theory and Mott insulators: Hubbard U instead of Stoner I*, Phys. Rev. B **44**, 943 (1991).

[139] V. I. Anisimov, F. Aryasetiawan, and A. I. Lichtenstein, *First-principles calculations of the electronic structure and spectra of strongly correlated systems: the LDA + U method*, Journal of Physics: Condensed Matter **9**, 767 (1997).

[140] V. I. Anisimov and O. Gunnarsson, *Density-functional calculation of effective Coulomb interactions in metals*, Physical Review B **43**, 7570 (1991).

[141] M. Cococcioni and S. de Gironcoli, *Linear response approach to the calculation of the effective interaction parameters in the LDA + U method*, Physical Review B **71**, 035105 (2005).

[142] S. Lany and A. Zunger, *Polaronic hole localization and multiple hole binding of acceptors in oxide wide-gap semiconductors*, Physical Review B **80**, 085202 (2009).

[143] P. Erhart, A. Klein, D. Åberg, and B. Sadigh, *Efficacy of the DFT + U formalism for modeling hole polarons in perovskite oxides*, Physical Review B **90**, 035204 (2014).

[144] A. D. Becke, *A new mixing of Hartree–Fock and local density-functional theories*, The Journal of Chemical Physics **98**, 1372 (1993).

[145] A. D. Becke, *Density-functional thermochemistry. III. The role of exact exchange*, The Journal of Chemical Physics **98**, 5648 (1993).

[146] A. D. Becke, *Density-functional thermochemistry. IV. A new dynamical correlation functional and implications for exact-exchange mixing*, The Journal of Chemical Physics **104**, 1040 (1996).

[147] V. Fock, *Näherungsmethode zur Lösung des quantenmechanischen Mehrkörperproblems*, Zeitschrift für Physik **61**, 126 (1930).

[148] J. P. Perdew, M. Ernzerhof, and K. Burke, *Rationale for mixing exact exchange with density functional approximations*, The Journal of Chemical Physics **105**, 9982 (1996).

[149] J. Heyd, G. E. Scuseria, and M. Ernzerhof, *Hybrid functionals based on a screened Coulomb potential*, The Journal of Chemical Physics **118**, 8207 (2003).

[150] J. Heyd, G. E. Scuseria, and M. Ernzerhof, *Erratum: "Hybrid functionals based on a screened Coulomb potential" [J. Chem. Phys.118, 8207 (2003)]*, The Journal of Chemical Physics **124**, 219906 (2006).

[151] B. Sadigh, P. Erhart, and D. Åberg, *Variational polaron self-interaction-corrected total-energy functional for charge excitations in insulators*, Physical Review B **92**, 075202 (2015).

[152] F. Gygi and A. Baldereschi, *Quasiparticle energies in semiconductors: Self-energy correction to the local-density approximation*, Physical Review Letters **62**, 2160 (1989).

[153] F. Bloch, *Über die Quantenmechanik der Elektronen in Kristallgittern*, Zeitschrift für Physik **52**, 555 (1929).

[154] D. R. Hamann, M. Schlüter, and C. Chiang, *Norm-Conserving Pseudopotentials*, Physical Review Letters **43**, 1494 (1979).

[155] D. Vanderbilt, *Soft self-consistent pseudopotentials in a generalized eigenvalue formalism*, Physical Review B **41**, 7892 (1990).

[156] P. E. Blöchl, *Projector augmented-wave method*, Physical Review B **50**, 17953 (1994).

[157] L. Hedin, *New Method for Calculating the One-Particle Green's Function with Application to the Electron-Gas Problem*, Physical Review **139**, A796 (1965).

[158] L. Hedin and S. Lundqvist, in *Solid State Physics*, edited by F. Seitz, D. Turnbull, and H. Ehrenreich (Academic Press, New York, New York, 1970), Vol. Volume 23, pp. 1–181.

[159] W. G. Aulbur, L. Jönsson, and J. W. Wilkins, in *Solid State Physics*, edited by H. Ehrenreich and F. Spaepen (Academic Press, San Diego, California, 1999), Vol. Volume 54, pp. 1–218.

[160] S. V. Faleev, M. van Schilfgaarde, and T. Kotani, *All-Electron Self-Consistent GW Approximation: Application to Si, MnO, and NiO*, Physical Review Letters **93**, 126406 (2004).

[161] M. van Schilfgaarde, T. Kotani, and S. Faleev, *Quasiparticle Self-Consistent GW Theory*, Physical Review Letters **96**, 226402 (2006).

[162] F. Fuchs, J. Furthmüller, F. Bechstedt, M. Shishkin, and G. Kresse, *Quasiparticle band structure based on a generalized Kohn-Sham scheme*, Physical Review B **76**, 115109 (2007).

[163] H. Jiang, R. I. Gomez-Abal, P. Rinke, and M. Scheffler, *Localized and Itinerant States in Lanthanide Oxides United by GW@LDA + U*, Physical Review Letters **102**, 126403 (2009).

[164] D. Åberg, B. Sadigh, and P. Erhart, *Electronic structure of LaBr$_3$ from quasiparticle self-consistent GW calculations*, Physical Review B **85**, 125134 (2012).

[165] W. Chen and A. Pasquarello, *Band-edge positions in GW: Effects of starting point and self-consistency*, Physical Review B **90**, 165133 (2014).

[166] C. Friedrich, M. C. Müller, and S. Blügel, *Band convergence and linearization error correction of all-electron GW calculations: The extreme case of zinc oxide*, Physical Review B **83**, 081101 (2011).

[167] C. Freysoldt, B. Grabowski, T. Hickel, J. Neugebauer, G. Kresse, A. Janotti, and C. G. Van de Walle, *First-principles calculations for point defects in solids*, Reviews of Modern Physics **86**, 253 (2014).

[168] C. W. M. Castleton and S. Mirbt, *Finite-size scaling as a cure for supercell approximation errors in calculations of neutral native defects in InP*, Physical Review B **70**, 195202 (2004).

[169] C. W. M. Castleton, A. Höglund, and S. Mirbt, *Managing the supercell approximation for charged defects in semiconductors: Finite-size scaling, charge correction factors, the band-gap problem, and the ab initio dielectric constant*, Physical Review B **73**, 035215 (2006).

[170] P. Erhart, B. Sadigh, A. Schleife, and D. Åberg, *First-principles study of codoping in lanthanum bromide*, Physical Review B **91**, 165206 (2015).

[171] M. Leslie and N. J. Gillan, *The energy and elastic dipole tensor of defects in ionic crystals calculated by the supercell method*, Journal of Physics C: Solid State Physics **18**, 973 (1985).

[172] G. Makov and M. C. Payne, *Periodic boundary conditions in ab initio calculations*, Physical Review B **51**, 4014 (1995).

[173] P. A. Schultz, *Charged Local Defects in Extended Systems*, Physical Review Letters **84**, 1942 (2000).

[174] S. Lany and A. Zunger, *Assessment of correction methods for the band-gap problem and for finite-size effects in supercell defect calculations: Case studies for ZnO and GaAs*, Physical Review B **78**, 235104 (2008).

[175] I. Dabo, B. Kozinsky, N. E. Singh-Miller, and N. Marzari, *Electrostatics in periodic boundary conditions and real-space corrections*, Physical Review B **77**, 115139 (2008).

[176] C. Freysoldt, J. Neugebauer, and C. G. Van de Walle, *Fully Ab Initio Finite-Size Corrections for Charged-Defect Supercell Calculations*, Physical Review Letters **102**, 016402 (2009).

[177] S. E. Taylor and F. Bruneval, *Understanding and correcting the spurious interactions in charged supercells*, Physical Review B **84**, 075155 (2011).

[178] Y. Kumagai and F. Oba, *Electrostatics-based finite-size corrections for first-principles point defect calculations*, Physical Review B **89**, 195205 (2014).

[179] J. Ihm, A. Zunger, and M. L. Cohen, *Momentum-space formalism for the total energy of solids*, Journal of Physics C: Solid State Physics **12**, 4409 (1979).

[180] H.-P. Komsa, T. T. Rantala, and A. Pasquarello, *Finite-size supercell correction schemes for charged defect calculations*, Physical Review B **86**, 045112 (2012).

[181] C. Persson, Y.-J. Zhao, S. Lany, and A. Zunger, *n-type doping of* $CuInSe_2$ *and* $CuGaSe_2$, Physical Review B **72**, 035211 (2005).

[182] D. Åberg, P. Erhart, A. J. Williamson, and V. Lordi, *Intrinsic point defects in aluminum antimonide*, Physical Review B **77**, 165206 (2008).

[183] H. Peng, D. O. Scanlon, V. Stevanovic, J. Vidal, G. W. Watson, and S. Lany, *Convergence of density and hybrid functional defect calculations for compound semiconductors*, Physical Review B **88**, 115201 (2013).

[184] R. Feynman, *Forces in Molecules*, Physical Review **56**, 340 (1939).

[185] L. Kantorovich, *Quantum Theory of the Solid State: An Introduction* (Springer Netherlands, Dordrecht, 2004).

[186] G. Henkelman and H. Jónsson, *Improved tangent estimate in the nudged elastic band method for finding minimum energy paths and saddle points*, The Journal of Chemical Physics **113**, 9978 (2000).

[187] G. Henkelman, B. P. Uberuaga, and H. Jónsson, *A climbing image nudged elastic band method for finding saddle points and minimum energy paths*, The Journal of Chemical Physics **113**, 9901 (2000).

[188] P. G. Sundell, M. E. Björketun, and G. Wahnström, *Thermodynamics of doping and vacancy formation in* $BaZrO_3$ *perovskite oxide from density functional calculations*, Physical Review B **73**, 104112 (2006).

[189] M. E. Björketun, P. G. Sundell, and G. Wahnström, *Structure and thermodynamic stability of hydrogen interstitials in* $BaZrO_3$ *perovskite oxide from density functional calculations*, Faraday Discussions **134**, 247 (2007).

[190] Z. Zhang, W. Sigle, F. Phillipp, and M. Rühle, *Direct Atom-Resolved Imaging of Oxides and Their Grain Boundaries*, Science **302**, 846 (2003).

[191] K. J. Dudeck, N. A. Benedek, M. W. Finnis, and D. J. H. Cockayne, *Atomic-scale characterization of the* $SrTiO_3$ $\Sigma 3$ $(112)[\bar{1}10]$ *grain boundary*, Physical Review B **81**, 134109 (2010).